Department of Precision and Microsystems Engineering

Towards a neutrally stable compressible metamaterial

Jeffrey Zhu

Report no	: 2024.015
Coach	: Dr. ir. G. Radaelli
Professor	: Prof. dr. ir. J.L. Herder
Specialisation	: Mechatronic System Design
Type of report	: Master Thesis
Date	: March 8, 2024

TU Delft Delft University of Technology

Challenge the future

Towards a neutrally stable compressible metmaterial

by

Jeffrey Zhu

Student Name	Student Number
Jeffrey Zhu	4694155

Supervisor: Dr. ir. G. Radaelli
Chair: Prof. dr. ir. J. Herder
Project Duration: September, 2022 - March, 2024
Faculty: Department of Precision Mechanism Design, Delft

TU Delft

Preface

This thesis marks the end of my student time at the TU Delft. I am very grateful for all the fun years, the cool things I got to experience, and the great people I've met. This might be the end of my academic career, but I will never stop learning.
This project was very challenging and I've learned a lot along the way and gained more confidence in my knowledge. This project would not have been possible without the help of Giuseppe Radaelli, my supervisor. Thank you, Giuseppe, for all the bi-weekly meetings and the interesting discussions. Those sessions were really helpful and fun.
Finally, I would like to thank my parents, brother, sister, and girlfriend for providing mental support along the journey. And of course, a shout-out to Hilmi and Joran for all the carpool sessions.

Jeffrey Zhu
Houten, March 2024

Contents

Preface i

1 Introduction 1

2 Literature review 3

3 Research paper 17

4 Conclusion 29

A Appendix A - Test setup design 30

B Appendix B - Combined optimisation case 33

C Appendix C - Other concepts and ideas 34
C.1 Concept 1 34
C.2 Concept 2 34
C.3 Concept 3 35
C.4 Alternative beam 35

D Appendix D - Sign switching Poisson's Ratio 37

E Appendix E- Matlab code 40
E.1 Objective function 40
E.2 Cross-section optimiser model 43
E.3 Function for creating a single unit cell 43
E.4 Function for creating metamaterial (unit cell tessellation) 46

1 Introduction

Metamaterials have attracted much attention in the last two decades due to their ability to possess unusual properties[7]. Their extraordinary properties are derived not from the materials they are made of but from their precisely designed geometric structures[14][17]. This gives metamaterials the ability to possess properties that are unusual and extreme compared to constituent materials.

Mechanical metamaterials are a subgroup of metamaterials that focus on motion, displacements, stresses, and mechanical energy[1]. For example, they can display negative stiffness behaviors[8][11], where the material compresses under tensile stress and expands under compressive stress, defying conventional material responses. Additionally, they can exhibit negative thermal expansion[19], contracting when heated rather than expanding as traditional materials do. Furthermore, the Poisson's ratio in these materials can be tailored to be positive, zero, or negative[19][2][9], allowing for expansion, neutral response, or contraction perpendicular to an applied force, respectively.

Mechanical metamaterials with nonlinear stiffness properties are captivating for their stiffness programmability[20], their potential in energy absorption applications [15], and their shape-morphing capabilities [18]. These nonlinear stiffness metamaterials can be classified into three types of stability, namely monostability, multistability, and neutral stability.

Monostable nonlinear stiffness metamaterials include metamaterials with constant force properties, also called Quasi-zero stiffness properties. This refers to metamaterials with a single minimum in their potential energy landscape. The corresponding stiffness characteristic is high stiffness transitioning to almost zero stiffness as the displacement increases to a certain level. A possible application for these metamaterials is vibration isolation[22][10].

Conversely, metamaterials with multistability introduce a framework where multiple equilibrium states are feasible, caused by the presence of multiple local minima within their potential energy landscape. This is typically achieved through the tessellation of bistable unit cells. The unit cells often consist of some variation of a beam with two equilibrium positions. These types of metamaterials could be used for energy absorption[4][6] and shape morphing[13].

On the other hand, neutral stability in metamaterials is also an intriguing feature. In theory, these structures maintain a constant potential energy across the energy landscape, indicating that they do not require a force to deform or remain deformed. Their ability to change and sustain different shapes without requiring energy makes them an important innovation in developing more energy-efficient technology. For example, in linear guidance systems, mechanisms with zero stiffness in one direction (the guiding direction) but high stiffness in others are required. Neutrally stable metamaterials could meet this requirement. Despite the intriguing nature of neutrally stable metamaterials, research in this area is noticeably scarce. Research by Mukhopadhyay et al.[12] showcases an origami-based tubular-shaped metamaterial. This metamaterial is based on a waterbomb crease pattern and can exhibit negative stiffness properties and near-neutral stability by changing the tesselation sequence and folding angle. Additionally, research by Cai et al.[3] designed a novel one-dimensional quasi-zero stiffness metamaterial. The unit cell of this metamaterial is made of an elastic positive stiffness element and two buckling beams with negative stiffness elements. The positive stiffness can be neutralized by the negative stiffness, leading to the quasi-zero stiffness behavior. Near-neutral stability can be achieved in the unit cell by applying a pre-load. However, the neutral stable behavior is within the boundaries of the unit cell, thus the displacement region of neutral stability will not increase for the metamaterial. All in all, in the current research, no general method was found for creating neutrally stable metamaterials.

This paper presents a novel method for achieving neutral stability in metamaterials. It proposes a novel unit cell design with constant force properties. This unit cell consists of an upper half and a lower half. The upper half is the mirrored version of the lower half, both made up of four spline-shaped beams that are designed to experience lateral torsional buckling (LTB), inducing a constant force behavior. By introducing pre-tension in both the upper and lower halves of the unit cell, the areas exhibiting constant force characteristics are aligned with one another. This alignment shifts the behavior from a constant force response to a zero-force state, thereby achieving a neutrally stable behavior.

The primary goal of this paper is to assess the feasibility of this approach for achieving neutral stability. To accomplish this, the unit cell is geometrically optimized and then subjected to tests that mimic the expected behavior of the metamaterial. The subsequent analysis of the force-displacement results from these tests serves as the foundation for determining the method's viability.

2

Literature review

Literature review: Mechanical metamaterials with nonlinear stiffness and their stable states

Jeffrey Zhu, Giuseppe Radaelli

Department of Precision and Microsystems Engineering, Faculty of Mechanical Engineering and Marine Technology, Delft University of Technology, The Netherlands

***Abstract*—Mechanical metamaterials is a branch of metamaterials that focuses on motion displacements, stresses, and mechanical energy. Although these materials can achieve displacements by external stimuli, not all can maintain a deformed shape after removing the external stimuli. This review provides a novel categorization for metamaterials with stable states and nonlinear stiffness characteristics. This categorization serves as a guide for understanding and applying stability strategies based on information from the literature. The main strategy used for multistability is compression-induced snap-through mechanisms. For neutral stable metamaterials, negative and positive stiffness elements, and origami-inspired structures are used. In addition, this review rates and compares the various strategies based on factors such as scalability, manufacturability, and support stiffness. Finally, it was identified that neutral stable metamaterials show potential for future research.**

I. Introduction

Metamaterials are materials structured from periodically arranged building blocks that are also known as unit cells [1]. The properties of metamaterials originate from the microstructure rather than the chemical composition, such as constituent materials [2]. This gives metamaterials the ability to possess properties that are unusual and extreme with respect to constituent materials.

Mechanical metamaterials is a branch of metamaterials that mainly focuses on motion, displacements, stresses, and mechanical energy [1]. In the field of mechanical metamaterials, there are designs for negative stiffness [3], negative Poisson's ratio [4], negative thermal expansion [5], and a combination of these indices [6]. Negative stiffness in this context refers to the decrease in force as the displacement increases when the structure is under a load. Although all of these materials can achieve displacements by external stimuli, such as mechanical force and heat [7], not all mechanical metamaterials can maintain a deformed shape after removing external stimuli. By introducing multi-stability and neutral stability it will be able to maintain the deformed shapes without external stimuli. This is desirable because it allows for shape retention, and since these materials do not require continuous energy input to maintain their deformed shape, they prove to be energy-efficient. Multi-stable structures possess multiple local minima on the potential energy landscape and thus can rest in multiple stable states. Neutrally stable structures possess a constant potential energy on the energy landscape. This means that no force is required to deform the structure or to keep the structure in the deformed position, hence they are often referred to as zero stiffness structures [8].

Various reviews on mechanical metamaterials can be found prior to this literature review. For instance, a review of flexible metamaterials was conducted by Bertoldi et al. [1] This review identifies the principles leading to properties like pattern and shape transformation in response to mechanical forces, unidirectional guiding of motion and waves, and reprogrammable stiffness. Furthermore, a review from Wu et al. [9] summarizes the current shape-morphing programming strategies for mechanical metamaterials, this includes heterogeneous material composition and structural instabilities. Another review by Kelkar et al. [10] made a classification of auxetic metamaterials and their configurations. Finally, other reviews on more specific metamaterial properties have been made by i.e. Wu et al. [11] which reviews the dynamic properties of mainly elastic and acoustic metamaterials, Al Rifaie et al. [12] that reviewed the use of mechanical metamaterials for vibration isolation and damping, and Zhai et al. [13] reviewed the use of origami and kirigami principles in the design and fabrication of mechanical metamaterials. Despite these valuable contributions in the literature, a comprehensive review focusing on geometrically configured mechanical metamaterials with stable states and nonlinear stiffness characteristics is currently lacking. While previous reviews have considered individual properties or principles, they have not explored in depth the role of geometric configurations, stability principles and their interplay in creating these materials.

The aim of this work is (i) to provide an overview of different geometrically configured mechanical metamaterials with nonlinear stiffness characteristics and their stable states, (ii) to find the principles for stability in those metamaterials, and (iii) to identify gaps in the literature for new research directions.

The paper is structured as follows. The methods for collecting relevant literature, categorizing literature, and rating the performance are described in section II The results of the categorization and performance overview will be shown in section III and discussed in section IV. Finally, section V concludes the literature review.

II. Method:Literature review,

Categorization and Performance overview

For this literature review, the Scopus database was searched using specific terms and Boolean operators (as shown in Table I) to identify relevant articles published before November 24, 2022. The search included different spellings and synonyms of the terms to maximize the number of relevant results. The results were then manually filtered to include only articles related to nonlinear stiffness characteristics.

TABLE I
Overview of search terms used. The columns are combined with OR Boolean operators, while the rows are combined with AND Boolean operators.

	AND		
OR	Metamaterial Meta-material Cellular material Lattice material Architected material Micro lattice	Force Programmable Bistable Bi-stable Multi-stable Multistable Zero stiffness Continuous equilibrium Constant potential energy Neutral stable	Displacement Stiffness

Afterward, the collected literature is categorized into two independent categories. This categorization is visualized in Figure 1. The first category is geometry, this category describes the geometry of metamaterials. Metamaterials come in all kinds of shapes. Some metamaterials' working principles can be explained by solely looking at the 2D planar configuration, the out-of-plane dimension of the structures is in those cases constant and less relevant. Other shapes can be derived from a 2D planar configuration but are merely curved into a cylinder or other zero-gaussian shapes. Non-zero-Gaussian shapes are also included such as spheres. Lastly, there are 3D configurations, these shapes have varying parameters in all three dimensions and are subdivided into origami-inspired metamaterials and non-origami-inspired metamaterials.

The second category describes the stability of metamaterials. In this category, a distinction is made between three types of stability. Firstly, metamaterials that are monostable. Monostable means that after a force is removed the metamaterial will return to its initial stable position. One could argue that every metamaterial which is not multistable or neutrally stable is monostable. To prevent over-saturating this sub-category solely metamaterials with negative stiffness and zero stiffness properties are considered. Secondly, metamaterials can have multi-stable displacement states. Multi-stability means that after removing a force, the metamaterial can maintain a finite number of positions which is different than the initial position. Lastly, there are neutrally stable metamaterials. Neutrally stable metamaterials have the property of zero stiffness and also require zero force to deform the material. Due to these properties, it can retain infinite stability positions.

Finally, a performance overview will be provided to compare the different metamaterials on their properties. In this performance overview, the stiffness characteristic will be shown,

	2D	2D embedded in 3D			3D	
	Planar	Cylindrical	Zero-Gaussian	Non-zero-Gaussian	Planar	Planar
Mono stable	5	2			3	2
Multi stable	6	2			3	4
Neutral stable	1				1	

Fig. 1. Categorisation of the literature

this describes the characteristic of the force-displacement graph of the metamaterial. To add, their working dimensions are also displayed in the overview. This shows how many working directions the metamaterial has. However, since the metamaterials have different shapes and sizes they will also be rated on their scalability and manufacturability. Scalability describes the ability to make the metamaterial smaller and manufacturability is the difficulty and effort required to manufacture the metamaterial. Many metamaterials are being tested in their intended working direction, however, they are not always stiff enough in the other degrees of freedom. Thus, the support stiffness is also rated. The ratings are performed by comparing the different metamaterials and giving them a score ranging from '++' to '- -'.

III. Results

A. Monostable - 2D planar configuration

This category mainly consist of metamaterials with Quasi-zero stiffness(QZS) properties. Quasi-zero stiffness is a force-displacement relationship where a flat range occurs. Within that range, no additional force is required to increase the displacement. Thus, for that range there is zero stiffness. The relationship is illustrated in Figure 2

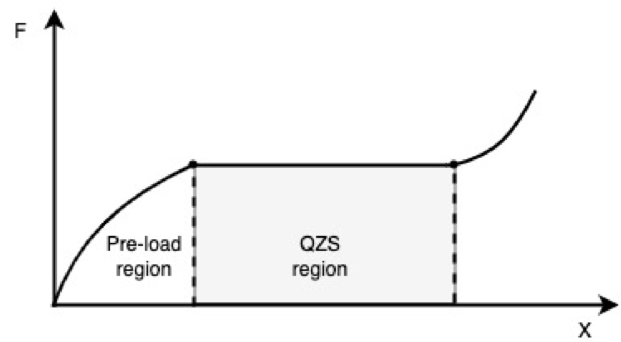

Fig. 2. Example of a force-displacement relation with QZS

In general, there are two types of QZS categories: combined-type and monolithic [14]. The combined-type configuration is made from unit cells with positive and negative stiffness elements, while the monolithic configuration is made from unit cells where the QZS property comes from a single element. Lin et al. [14], Zhou et al. [15], and Zhang et al. [16] designed a monolithic variant using a folded slender beam to achieve the QZS property. They conducted a folded slender beam optimization to determine the geometries of the slender beam. An example of the optimized unit cell can be seen in Figure 3.

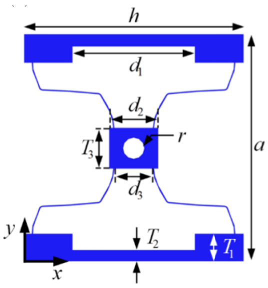

Fig. 3. Unit cell of a monolithic QZS unit cell. Retrieved from [15]

The unit cells can be arranged in different ways to create differently structured metamaterials. These arrangements include lateral arrangements, combined lateral and longitudinal orientations, or a pyramid-like stacking structure. As shown in Figure 4,Figure 5, and Figure 6, respectively. In the pyramid stacked configuration, the QZS behavior occurs periodically in the force-displacement relation. This is due to the uneven number of unit cells on each layer, which causes the required force to deform the layers to be unequal. When an increasing force is applied, the upper layer deforms past the QZS region first, followed by the middle layer, and finally the bottom layer. This deformation is also shown in Figure 6

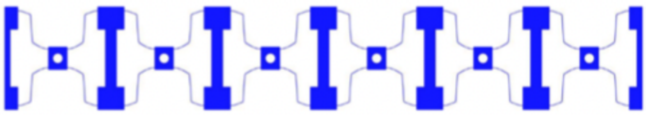

Fig. 4. Metamaterial with laterally arranged unit cells. Retrieved from [15]

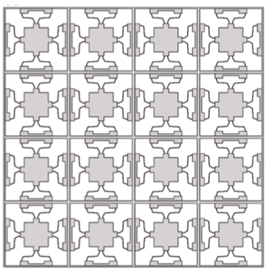

Fig. 5. Metamaterial with laterally and longitudinally arrange unit cells. Retrieved from [14]

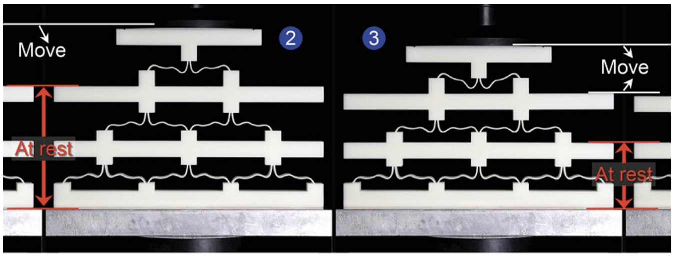

Fig. 6. Metamaterial with pyramid-like stacked unit cells. Retrieved from [16]

Cai et al. [17] and Fan et al. [18] designed a metamaterial with combined-type QZS-configured unit cells, shown in Figure 8. In both designs, the negative stiffness elements are designed to exhibit snap-through buckling behavior with bi-stable positions. In contrast, the positive stiffness element behavior can be represented as a spring with constant stiffness. Figure 7 shows the negative stiffness and positive stiffness elements in the force-displacement curve. Combining these two stiffness lines results in a QZS curve similar to Figure 2.

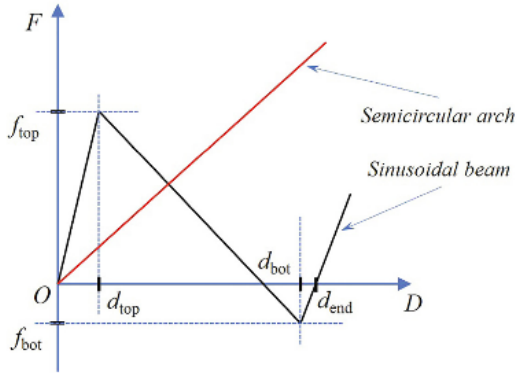

Fig. 7. Force-displacement relationship of positive and negative element. Retrieved from [18]

For the metamaterial, unit cells are arranged laterally and/or longitudinally, as shown in Figure 8. This arrangement of unit cells does not change the overall force-displacement behavior, except for a wider QZS range.

B. Monostable - Cylindrical configuration

Zolfagharian et al. [19] designed QZS cylindrical metamaterials with several variations as shown in Figure 9. Two different unit cells are used to create the variations, one unit cell is 'soft' and the other is 'stiff'. Except for the difference in stiffness, the stiff unit cell also exhibits a hardening behavior while the soft unit cell possesses a softening behavior [19]. This means that the stiff unit cell increases in stiffness after a certain point while the soft unit cell has decreasing stiffness. Making the metamaterial out of only one type of unit cell will lead to global buckling instabilities which are unwanted. By employing soft and stiff unit cell configurations along with multi-thickness walls, we can densify the cylindrical

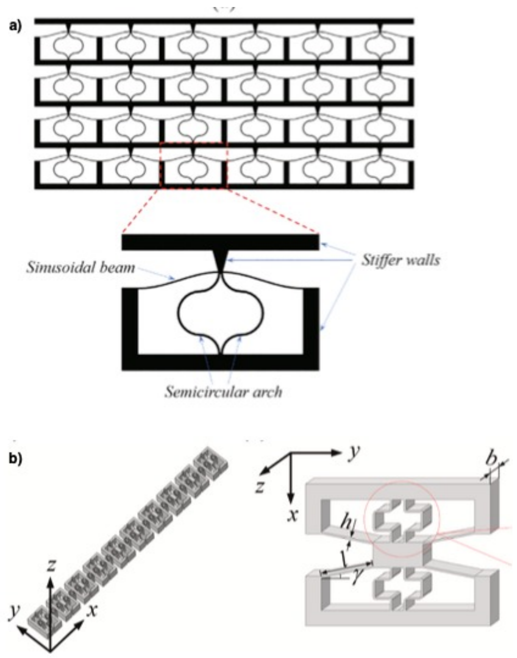

Fig. 8. a) Unit cell design of Fan et al. [18] b) unit cell design of [17]

metamaterial layer-by-layer, thereby preventing the occurrence of global buckling. The unit cells are stacked along a single direction to create the metamaterials. All models show a QZS behavior, however, models 1 and 4 show a larger stiffness than models 2 and 3.

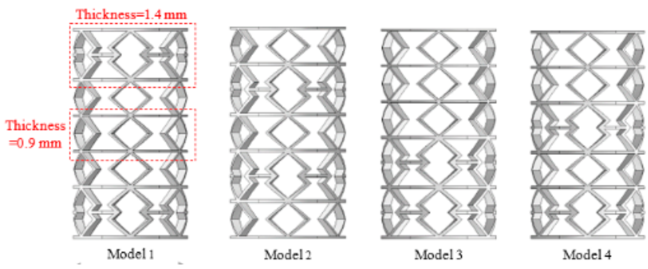

Fig. 9. Cylindrical monostable metamaterials. Retrieved from [19]

In addition, another cylindrical metamaterial by Wang et al. [20] is chiral and has negative stiffness properties. Chirality is described as the inability of an object to coincide with its mirror image and one of the basic properties is negative Poissons' ratio [20]. The unit cells of this metamaterial consist of tape springs as shown in Figure 10. That is also where the negative stiffness property originates from. Besides, stiffness of the unit cell increases with the increase of the concave angle of the tape spring. The metamaterial is illustrated in Figure 11.

C. *Monostable - 3D origami-inspired configuration*

In recent years origami has aroused great interest from engineers and mathematicians, due to its special characteristics

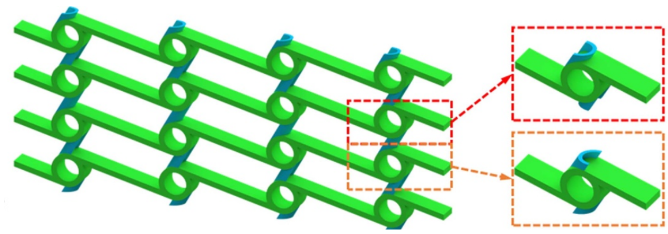

Fig. 10. 2D stacked chiral unit cell. Retrieved from [20]

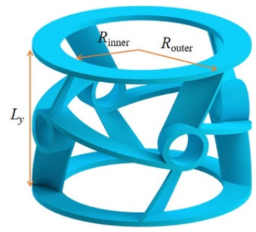

Fig. 11. Chircal metamaterial. Retrieved from [20]

and wide application prospects. Studies revealed that origami-based mechanical metamaterials possess unique properties that traditional mechanical metamaterials do not have [21]. The most studied origami-based metamaterials are based on Miura origami, shown in Figure 12. The Miura origami is on itself a mechanical metamaterial with a negative Poissons' ratio for in-plane deformations and a positive Poissons' ratio for out-of-plane deformations. [21]

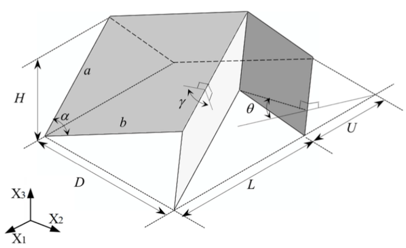

Fig. 12. Miura-ori unit cell. Retrieved from [22]

First consider the stacked Miura-ori metamaterial shown in Figure 13. The unit cells are not individually glued or connected to each other but are folded out of a single paper sheet. There are two variants of this metamaterial. One with uniform unit cells and one with unit cells varying in folding angle. The deformation mechanism of the uniform metamaterial is mainly dominated by the origami motion mechanism, while the non-uniform metamaterial it is more complex. In the case of the non-uniform metamaterial, the smallest cells collapse first due to their low initial collapse strength, but their final collapse strength is the highest. Despite their different deformation mechanisms, the overall responses are similar. Both show QZS behavior.

Another variant of the Miura-ori unit cell is a zigzag-based stacked-origami (ZSBO) [21]. This unit cell is made

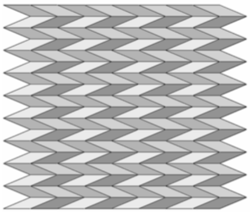

Fig. 13. Stacked uniform Miura-ori metamaterial [22]

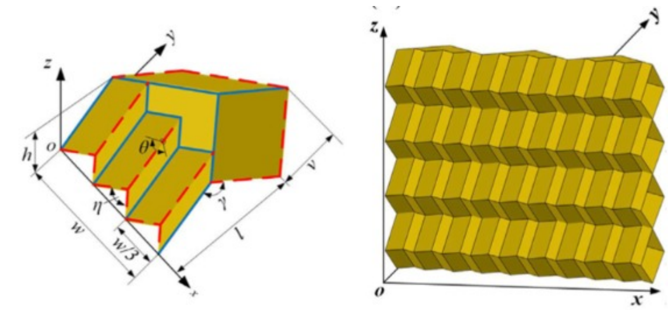

Fig. 14. ZSBO unit cell (left) and the metamaterial (right). Retrieved from [21]

by adding additional creases to a classical Miura-ori fold. The metamaterial shows different force-displacement behaviors depending on how many creases and on which side the creases are added because the creases change the stiffness of the unit cell. In general, the metamaterial shows a multistage stiffness behavior, with periods of increasing stiffness followed by negative stiffness. When compressing, the unit cells will deform until a certain point where snap-through instabilities occur that cause negative stiffness. In this paper, the ZSBO metamaterial deformed permanently in the final state, so it cannot be used to achieve the mechanical properties under cyclic loading. However, this could be prevented by using a hyperelastic material as the constituent material.

In addition, the metamaterial by Kamrava et al. [23] is also based on the Miura-ori unit cells as shown in Figure 15. Two unit cells are positioned in a zigzag pattern and then mirrored to create a symmetric structure, known as the "first-order element." These first-order elements are then arranged to form the metamaterial, illustrated in Figure 16. The metamaterial is monostable, but it can exhibit negative stiffness behavior depending on the angles of the unit cell α and θ. It exhibits negative stiffness behavior under out-of-plane loading for $\theta \geq 155°$ and under in-plane loading for $\theta \leq 40°$, when $\alpha = 60$.

Fig. 15. Zigzag patterned Miura-ori unit cell. Retrieved from [23]

Fig. 16. Metamaterial of the Zigzag patterned Miura-ori unit cell. Retrieved from [23]

D. Monostable - 3D non-origami-inspired configuration

Metamaterials found for this category have the ability to exhibit negative stiffness, which can be either monostable or multi-stable. The type of negative stiffness behavior exhibited by these metamaterials is influenced by the geometric ratios of the unit cell.

In the case of the monostable buckling beams, the unit cell consists of four components: four caps, six double-curved beams, four near-rigid columns, and one skeleton [24]. This is shown in Figure 17a. The caps are used to immobilize the skeleton and double-curved beams. The key component is the two-curved centrally-clamped parallel beams because this component is responsible for the snap-through negative stiffness behavior. Using double-clamped beams prevents it from twisting therefore the motion is restricted to only one direction. Whether the unit cell is monostable or bistable depends on the geometric ratio of $Q = \frac{h}{t}$. This is the ratio between the deflection of the beam to the middle line and the thickness of the beam.

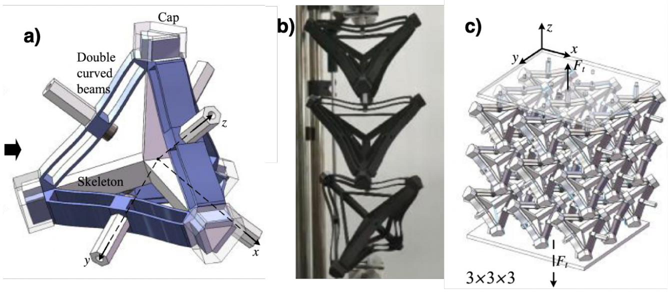

Fig. 17. a) Double-curved beams unit cell. b) 3x1x1 unit cell configuration. c) 3x3x3 unit cell configuration Retrieved from [24].

To create the metamaterial, the unit cells are placed in 3x1x1 and 3x3x3 configurations, shown in Figure 17b and c. The number of unit cells affects the overall energy dissipation behavior. Additionally, the 3x3x3 configuration of the metamaterial allows for tri-directional energy dissipation due to its negative stiffness behavior in the X, Y, and Z directions. While for the 3x1x1 configuration the negative stiffness behavior acts only in one direction. The unit cell is monostable for $Q < 2.31$.

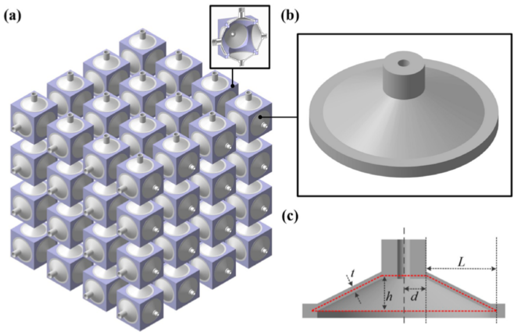

Fig. 18. 3x1x1(left) and 3x3x3(right) metamaterial configuration. Retrieved from [25]

In the case of the conical shell, shown in Figure 18, the negative stiffness behavior is exhibited by the cone-shaped structure. The conical shells are placed on each face of a cube to create the unit cell. The mechanical responses are influenced by the height, thickness, and internal and external diameter [25]. The stability of the unit cell was sensitive to the height-span ratio, but no specific value was mentioned in the paper. The metamaterial is structured by arranging the unit cells in three directions, allowing the material to move in three directions.

E. Multi-stable Planar configuration

Multi-stable metamaterials are often made out of bistable unit cells. The most common type of unit cell designs makes use of buckling beams, such as the designs in Figure 19. Restrepo et al. [26] and Tan et al. [27] both made use of curved beams, shown in Figure 19a and c respectively. In the design of Restrepo et al. [26] a sinusoidal beam was used. The sinusoidal beams act as compliant bistable mechanism, while the stiffening walls provide local support to prevent transverse displacement at the ends of the sinusoidal beams. The metamaterial is composed of an array of sinusoidal beams that are connected in series to form mechanism chains and multiple chains are stacked on top of each other. The stacking arrangement is similar to the one in Figure 8a. When a load is applied to the metamaterial, it exhibits a linear stress-strain response until the first row of sinusoidal beams collapses, leading to a new stable position. The effective stiffness of the metamaterial is dependent on the stiffness of the sinusoidal beams and the number of sinusoidal beams in a chain. Adding more beams or chains decreased the effective stiffness.

Tan et al. [27] on the other hand created the curved beam by pre-compressing laterally. The pre-compression is imposed by using spacer pins that are fixed on the stiff walls of the unit cell. The stretchability is tunable by changing the lateral compression. An increase in compression leads to an increase in the longitudinal dimension. The unit cells are also arranged longitudinally and laterally just like the metamaterial of Restrepo et al. The metamaterial snaps through row by row, however, the deformation sequences are unpredictable. The unit cell design was also modified by replacing the spacer with

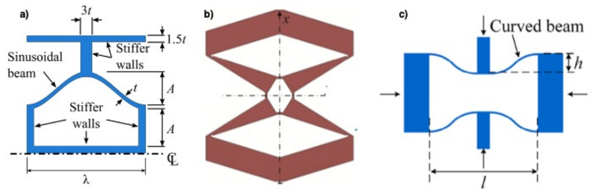

Fig. 19. a) Unit cell constructed with sinusoidal beams. b) Unit cell constructed with V-shaped triangles. c) Unit cell constructed with curved beams. Retrieved from [26], [28] and [27] respectively.

a stiffer curved beam, shown in Figure 20. Two of these stiffer curved beams are placed between the two stiff walls of the unit cell. The beams are heated and pre-compression is applied, causing them to bend and maintain the pre-compressed state when cooled.

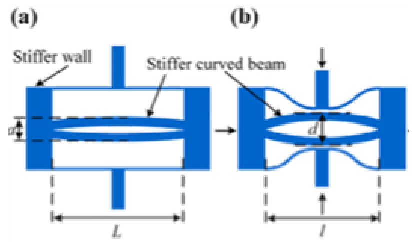

Fig. 20. Adjusted pre-compressed unit cell. Retrieved from [27]

Furthermore, the unit cell shown in Figure 19b by Ma et al. [28] uses V-shaped triangles to achieve bistability via snap-through behavior. The triangles are narrower at the point of connection such that is can deform in the narrow sections, acting like hinges. The unit cells are arranged in both horizontal and vertical directions. And the metamaterial deforms layer by layer.

Besides, the unit cells shown in Figure 21a also use bistable triangular frames to achieve bistability, while the unit cell in Figure 21b makes use of a hinge mechanism to achieve multistability. With these unit cells, a wide variety of metamaterials can be constructed allowing multi-degree-of-freedoms and multistability in 2d and 3d [29]. However only, two planar variants of the metamaterials were tested. Figure 22 shows two different metamaterials, both can have horizontal and vertical deformations but each is constructed with a different unit cell. The difference between the two metamaterials constructed with the multistable unit cell can achieve large displacements with a relatively small load, while the other metamaterial requires a larger load.

Additionally, metamaterials with triple-negative-index (negative Poissons' ratio, negative stiffness, and negative thermal), double-negative-one-zero-index(negative stiffness, negative thermal expansion, and zero Poissons' ratio), and double-zero-one-negative-index(zero Poissons' ratio, zero thermal expansion, and Negative stiffness) were designed by Yang et al. [30] The bistability in the unit cells and the multistability of the metamaterial are also created by pre-compressed curved

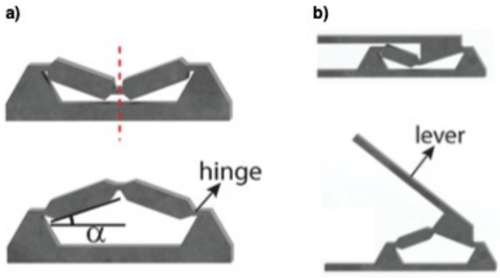

Fig. 21. a) Bistable unit cell. b) Multistable unit cell. Retrieved from [29]

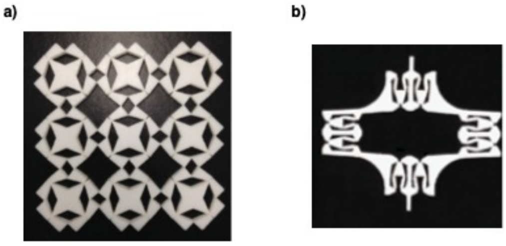

Fig. 22. a) Metamaterial made from bistable unit cell. b) Metamaterial made from multistable unit cell. Retrieved from [29]

beams. The other index properties of the metamaterial however originate from the design of the stiffer framework and the unit cell arrangement. There are two types of frameworks for the unit cells: a hexagonal one and a square one shown in Figure 23. The triple-negative-index metamaterial is made from the hexagonal unit cell in the compressed state, shown in Figure 24a. The rectangular unit cells provided the double-negative-one-zero-index and double-zero-one-negative-index metamaterials. Arranging the rectangular unit cells differently leads to different properties. The rectangular arrangement, shown in Figure 24b, can have zero thermal expansion property. While, arranging the unit cells at an angle, shown in Figure 24c, can lead to negative thermal expansion property.

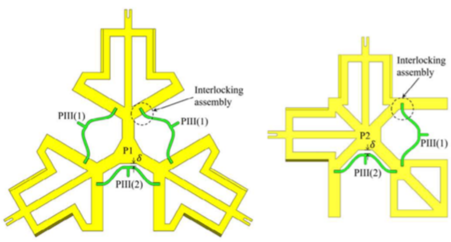

Fig. 23. Unit cells with hexagonal and rectangular framework. Retrieved from [30]

Lastly, a unit cell design by Niknam et al. [31] made use of thermal softening behavior to control the bistability, shown in Figure 25. When a certain compressive load is applied the unit cell will retain its deformed stable position. The principle behind this is again the use of beams that exhibit negative stiffness behavior. The unit cell can restore to its initial position when the temperature surpasses a critical value. At lower temperatures, the beams will soften which allows the beams to snap back to the initial position. While at higher temperatures the stiff walls will soften which allows lateral movement for the beams and no snap-back behavior will occur, making the unit cell monostable. The unit cells can be arranged vertically with smaller units on top of each other or horizontally. The vertical arrangement collapses layer for layer leading to multistability, while the horizontal arrangement is bistable because the row deforms simultaneously.

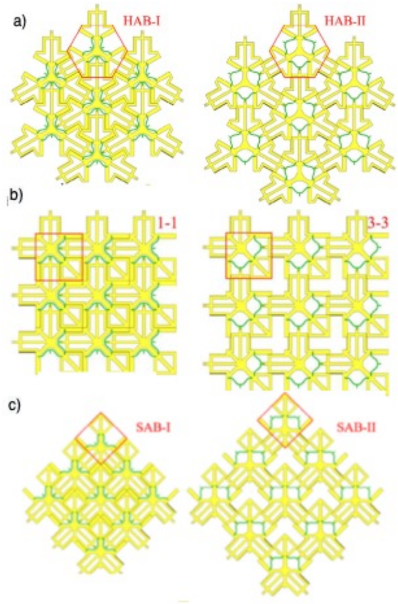

Fig. 24. a) Metamaterial made from hexagonal unit cells. b) Metamaterial made from rectangular unit cells arranged rectangularly. c) Metamaterial made from rectangular unit cells arranged at an angle. Retrieved from [30]

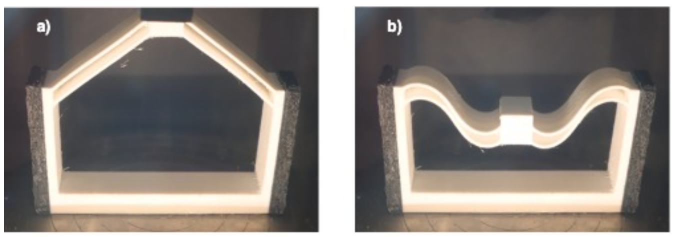

Fig. 25. Bistable thermal unit cell. a) Initial position. b) Deformed stable position. Retrieved from [31]

F. Multi-stable Cylindrical configuration

Ma et al. [28] also designed a cylindrical metamaterial. The cylindrical unit cell is the same as the planar one shown in Figure 19b, but it is convolved with a bending angle θ. The peak force in the force-displacement curve tends to increase for a decreasing θ and saturates when θ increases. Moreover, the bistability in the cylindrical unit cell configuration is weaker than in the planar configuration because less force is required to restore the initial position.

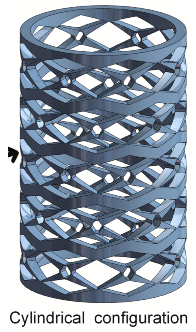

Fig. 26. Cylindrical configuration of the metamaterial. Retrieved from [28].

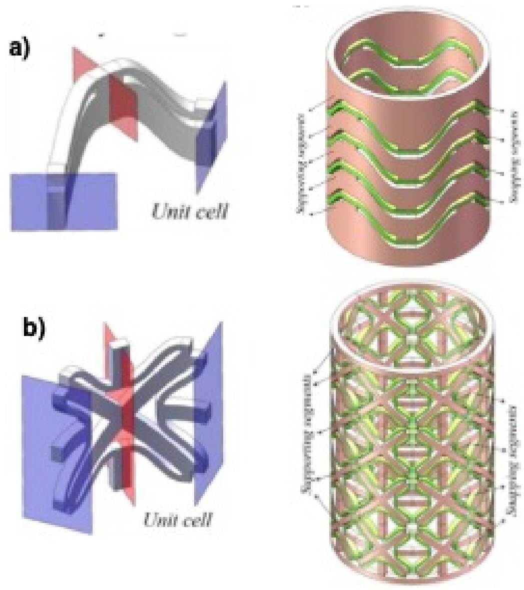

Fig. 27. a) One direction bistable unit cell. b) Two direcitions bistable unit cell. Retrieved from [32]

In a study by Yang et al. [32], two cylindrical metamaterial designs were presented. One of the designs was multistable in the longitudinal (1D) direction, while the other was multistable in both the longitudinal and radial directions (2D). The unit cells of both designs are shown in Figure 27. It is worth noting that curved beams were used to achieve negative stiffness behavior in these designs. Unlike other metamaterials, these designs were tested under tensile loading. The mechanical responses of both metamaterials were similar, with the snapping forces increasing under tensile loading and decreasing under compression loading. However, the stability in the 1D metamaterial appeared to be stronger, meaning that it requires more energy to transition from one stable state to another.

G. Multistable - 3D origami-inspired configurations

Previously, several monostable Miura-ori-inspired metamaterials were shown. Another miura-ori inspired metamaterial was designed by Kamrava et al [33]. The unit cells are built by folding a Miura-ori string. This is a sequence of n individual Miura-ori. The crease pattern of the string is defined by the number of Miura-ori(n), the characteristic angles α_1 and α_2 with $\alpha_1 > \alpha_2$, and the dimensions a and H shown in Figure 28.

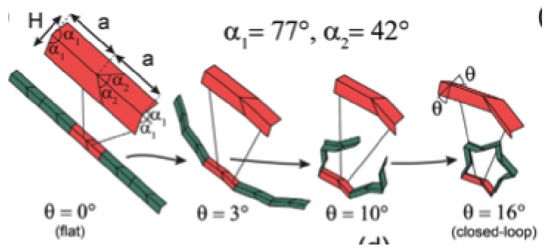

Fig. 28. The Miura-ori string. Retrieved from [33]

The stability of the unit cell depends on the characteristic angles, the unit cell can be monostable and bistable. Varying the parameter n allows the creation of different unit cell shapes, as illustrated in [Figure 29]. These different unit cells can be stacked on top of each other to form metamaterials as shown in Figure 30a. Due to the auxetic property of the unit cells, the metamaterials have a decrease in cross-sectional area and volume in the final stable state. However, the unit cells can also be arranged differently to create a metamaterial that allows multistability in two directions shown in Figure 30b. This metamaterial is created by placing three different types of bistable unit cells along the X-axis, one type of bistable unit cell along the Y-axis, and one monostable unit cell along the Z-axis.

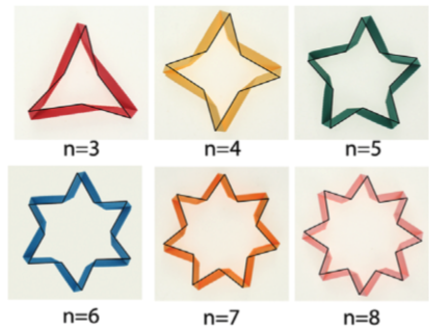

Fig. 29. Different Miura-ori strings shapes. Retrieved from [33]

Research by Liu et al. [34] presented a multi-stable origami pattern, named the shrimp pattern. The geometry is inspired by the segmented structure of a shrimp, hence the name. The unit cell switches from stable states by snap-through behavior. The unit cell is created by modifying the geometry of a rigid foldable pattern to block a range of kinematics, which can only be overcome by non-rigid origami deformations, illustrated in Figure 31. This separation of rigid and non-rigid kinematics allows the shrimp pattern to display both types of origami behavior. In reality, the flexibility of materials allows the Shrimp pattern to transition between its two rigid origami configurations through non-rigid deformation. The tail panels are added to allow the blocked range to be overcome without

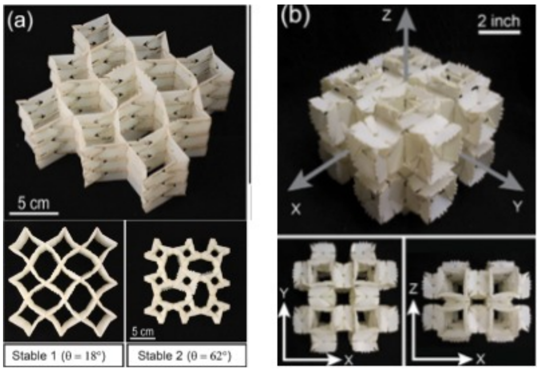

Fig. 30. a) Metamaterial with stability in one direction. b) Metamaterial with stability in two directions. Retrieved from [33]

damaging the material. Together, the addition of these panels leads to bistable snapping between the two parts of the rigid origami configuration of the Shrimp pattern. Figure 32 shows the various stable states of the metamaterial.

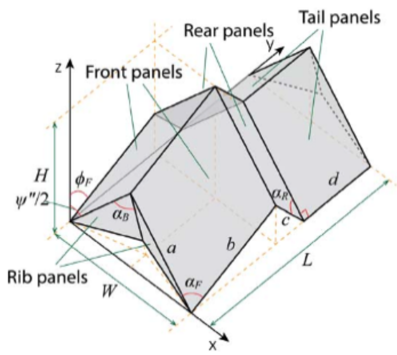

Fig. 31. Shrimp pattern unit cell. Retrieved from [34]

Fig. 32. Shrimp pattern metamaterial and its stable states. Retrieved from [34]

Another origami-inspired metamaterial is the hypar chain by Filipov et al. [35]. The origami hypar is made by using a square sheet and creasing it along diagonal lines that cross in the center of the sheet. Concentric perimeter folds are then added, starting from the outside and working toward the center. The fold polarity (mountain or valley) is alternated as the folds are added. The hypar does not have uni-directional folding motion like most other unit cells. Instead, the hypar deforms in a way that is similar to two von-Mises trusses. As the system changes between stable states, the points where the support and load are applied move outward. This deformation is shown in Figure 33. Local sequential and perimeter buckling does occur which results in force jumps in the force-displacement response. For the metamaterial, the hypars are connected on top of each other so it forms a chain. The metamaterial shows multistability through global sequential snap-through behavior. However, the deformation is not smooth and local deformations in the unit cells occur when the system transitions between stable states.

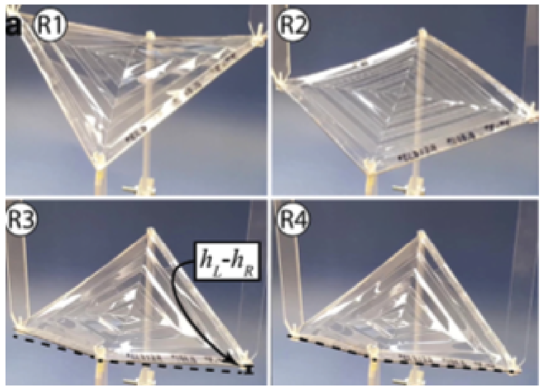

Fig. 33. Hypar unit cell. Retrieved from [35]

H. Multistable - 3D non-origami-inspired configurations

In subsection III-D we have presented the monostable variants of the double curved beam [24] and conical shells metamaterial [25], shown in Figure 17 and Figure 18. Their stability depends on their geometric ratios. For the double curved beam unit cell, bistability occurs when $Q = \frac{h}{t} > 2.31$. The bistability becomes stronger with increasing Q. For the conical metamaterial, the stability depends on the height-span ratio.

Another metamaterial design by Ma et al. [28] was also based on the unit cell shown in Figure 19b. The stereometric configured unit cell of this design can be obtained by rotating the planar unit cell in by $90°$. This results in the unit cell and metamaterial shown in Figure 34. The bistability of this metamaterial is shown to be stronger than the planar variant. With a compression load, the metamaterial also deforms layer by layer like the planar and cylindrical variants.

Furthermore, research by Ma et al. [36] provided a unit cell design for a potential metamaterial. Herein the unit cell is a modular system that is composed of three different types of base mechanisms: two planar mechanisms and one spatial mechanism, illustrated in Figure 35. The planar mechanisms are designed to have different ranges of the radius when they move individually. When the ranges overlap, the unit cell is kinematically compatible and moves like a mechanism. However, when there is a difference in radius between the two planar mechanisms, the unit cell becomes incompatible and

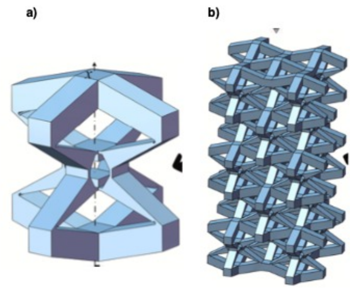

Fig. 34. a) Stereometric unit cell. b) Stereometric metamaterial. Retrieved from [28]

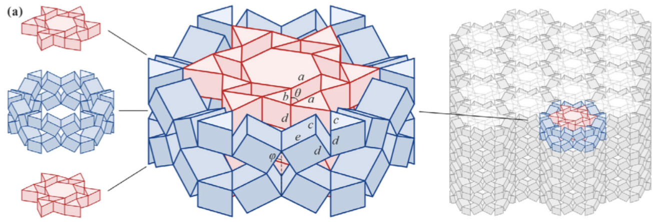

Fig. 35. Modular unit cell. Retrieved from [36]

requires some structural deformation, in order to maintain the connection between the base mechanisms. As a result of this design, the unit cell exhibits bistable behavior, with two extended quasi-stable regions rather than two stable states. This means that the unit cell can be in one of two different stable configurations, and it requires a relatively large force to switch between these configurations. The deformation sequence is shown in Figure 36. No metamaterial was constructed in this paper but it was mentioned the unit cell can also be tessellated in space to form a metamaterial with similar bistable performance.

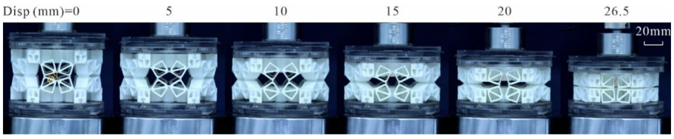

Fig. 36. Deformation sequence of the modular unit cell. Retrieved from [36]

Moreover, a perforated shellular unit cell was introduced by Shi et al. [37]. Shellulars are composed of periodic 3d unit cells of continuously smooth and curved shells. The unit cell design is based on Schwarz's Primitive surface. This surface however is monostable, but by applying perforations to the surface it can become bi-/multistable. Two perforation strategies are used to create bi-/multistability. The first strategy involves the use of elliptical holes to create bistable shellular unit cells. The bistability of these materials arises from the balance between compression-induced buckling and bending of the flexible parts of the structure. The second strategy involves the use of multilayer staggered perforations that form hinges and ease local instabilities to create multistable shellular unit cells. With n-layer staggered perforations, a maximum of 2^{n-1} stable states can be achieved in each shellular unit cell. The unit cells can be arranged as shown in Figure 38 to get the metamaterial. The metamaterial is multistable in three directions. Also, other arrangements and variations can be made to make the metamaterial one or two-directional multistable.

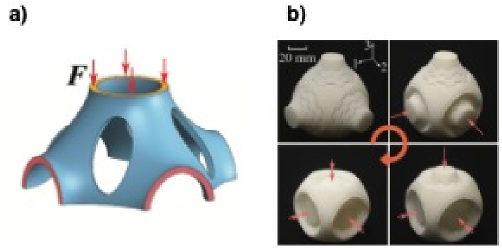

Fig. 37. a) Elliptical perforated unit cell. b) Multilayer staggered perforated unit cell. Retrieved from [37]

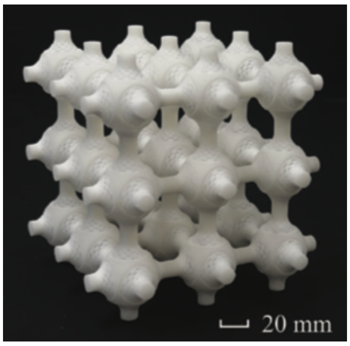

Fig. 38. Metamaterial composed of staggered perforated unit cells. Retrieved from [37]

Lastly, a wire shaped metamaterial, called the metawire, by Liu et al. [7] can also achieve multistability. This metamaterial is shaped like a wire with crease-connected truncated cones as unit cells. Figure 39 shows the unit cell and the stable states. The metawire is made up of units that have three basic stable states: deployed, retracted, and bent. These units can be combined into a metamaterial in different ways to create complex 2D or 3D stable configurations.

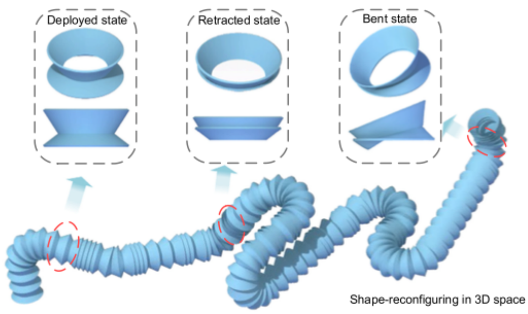

Fig. 39. Stables states of the unit cells and the metawire. Retrieved from [7]

I. Neutral stable - planar configuration

The design QZS from Figure 8c by Cai et al. [17] could also be tuned such that it has a near-zero force region. Within that displacement region almost zero force is required to make deform the metamaterial. However, when it moves outside that range the stiffness increases steeply.

J. Neutral stable - 3D origami inspired configuration

Here an origami-based metamaterial by Mukhopadhyay et al. [38] is able to achieve near zero stiffness, thus almost neutral stable. The metamaterial is based on a tubular waterbomb geometry. The waterbomb crease pattern is shown in Figure 40 with the red marked square being the unit cell. Unlike other metamaterials where the overall force-displacement response does not change drastically, this metamaterial does show a change in behavior for increasing numbers of unit cells. Two variants of the metamaterial are shown in Figure 41, one with 7 rows(m=7) and 12 unit cells per row(n=12) and one consisting of 9 rows with 30 unit cells per row. Both initial shapes are tubular, but their final shapes differ a lot. Also, it is notable that one metamaterial has near-zero stiffness for the whole deformation path while the other is only near zero stiff for a part of the deformation. The reason that it differs is due to the energy conservation of the system. The total applied energy is equal to the sum of energy required due to the rotation(opening and closing) of all folds in the system. So when a compression load is applied some folds open up and some folds close. In the case of the metamaterial in Figure 41 the amount of energy needed to close a fold and to open a fold is equal till a certain point. From that point on a net positive amount of energy is needed to deform the system.

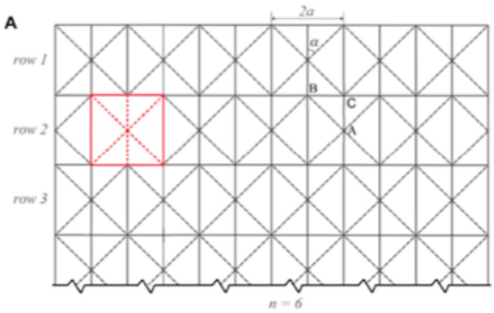

Fig. 40. Tubular waterbomb crease pattern and unit cell. Retrieved from [38]

K. Performance Overview

The performances are estimated and rated shown in Table II.

IV. Discussion

Rating the results on their performances makes the comparison between metamaterial easier. What is noticeable is that, in general, the scalability and manufacturability of planar metamaterials are better. Scalability and manufacturability are related to a certain extent because often easy to manufacture designs can also be scaled down more easily. Conversely,

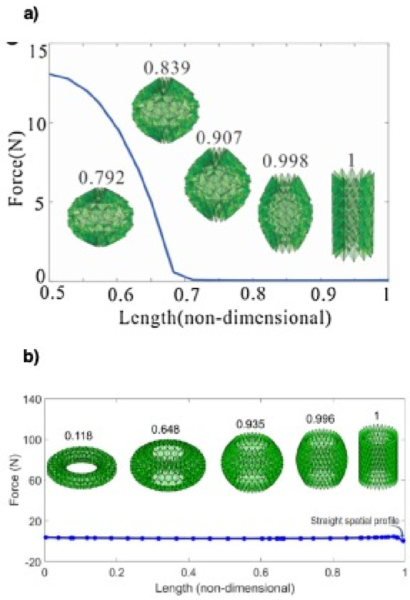

Fig. 41. Two variant of the metamaterial. a) Metamaterial with m=7 n=12. b) Metamaterial with m=9 n=30. Retrieved from [38]

origami metamaterials score the lowest on scalability and manufacturability because the folds are harder to realize when the geometry is scaled down. In addition, planar metamaterials have relatively bad support stiffness in the non-intended working direction. Mainly stiffness in the out-of-plane rotation is weaker. Origami metamaterials also have worse stiffness in other directions because they are often made of paper. However, that could be improved by changing the constituent material. Cylindrical and 3D metamaterials show greater support stiffness. So slightly changing and arranging planar unit cells could improve the support stiffness, as shown by Ma et al. [28]. While the ratings focused on the absolute stiffness of different metamaterials, it's worth noting the limitations inherent in this approach. Comparing absolute stiffness values doesn't necessarily provide a comprehensive picture of a material's overall performance characteristics. In particular, it fails to capture the importance of relative stiffness, which considers the relationship between stiffness in one direction to another direction. Unfortunately, the existing literature primarily focuses on absolute stiffness, which means the data necessary to compare metamaterials on relative stiffness is largely absent

Furthermore, all multistable metamaterials have negative stiffness properties. In general, this property is realized through some compression-induced snap-through behavior. The most common method to realize snap-through behavior is through curved buckling beams. In the case of origami-inspired designs, most designs are inspired by the well-known Miura-ori fold. Monostable metamaterials on the other hand can also possess QZS properties. This can be realized by either combining a negative stiffness and positive stiffness element or by designing a single monolithic element that has QZS

TABLE II
PERFORMANCE OVERVIEW OF ALL METAMATERIALS

Metamaterial concept	Scalability	Manufacturability	Support stiffness	Stiffness characteristic	Working dimensions
Monostable planar:					
[15], [16], [17], [18]	++	++	- -	QZS	1D
[14]	++	++	- -	QZS	1D
Monostable cylindrical:					
[19]	+	+	++	QZS	1D
[20]	+	+	++	NS	1D
Monostable origami-inspired:					
[21]	-	-	-	NS	1D
[22]	- -	-	- -	NS	2D
[23]	- -	-	- -	NS	1D
Monostable 3D:					
[24]	- -	- -	+	NS	1D
[25]	+	+	++	NS	3D
Multistable planar:					
[26], [28]	++	++	-	NS	1D
[27]	-	+	-	NS	1D
[29]	++	++	-	NS	2D
[30]	+	-	-	NS	2D
[31]	++	++	-	NS	1D
Multistable cylindrical:					
[28]	+	+	++	NS	1D
[32]	+	+	++	NS	2D
Multistable origami inspired:					
[33]	- -	- -	+	NS	2D
[34]	- -	-	- -	NS	1D
[35]	-	-	- -	NS	1D
Multistable 3d					
[28]	-	+	+	NS	1D
[36]	- -	-	++	NS	1D
[37]	-	+	+	NS	3D
[7]	+	+	++	NS	3D
Neutral stable planar [17]	++	++	- -	zero stiffness	1D
Neutral stable origami inspired [38]	- -	-	+	zero stiffness	1D

properties. While combining positive and negative stiffness elements can be used to create QZS stiffness metamaterials, it can also be used to create neutral stable metamaterials. Also, origami can be a method to create near-neutral stable metamaterials. To achieve near-neutral stability, it is essential to ensure a redistribution of strain energy within the system. This redistribution entails maintaining a balance between the energy released through negative stiffness and the energy absorbed by positive stiffness [38]. Moreover, most metamaterials are designed for 1-dimensional displacements. But adjusting and arranging the unit cell slightly differently could increase the number of displacement dimensions, the design by Shi et al. [37] and Tan et al. [25] are some examples.

Improvements in the search for literature could also be made. For the literature compilation process, all search queries included the word 'metamaterial' and its synonyms. However, it is worth considering whether this approach inadvertently excludes potentially promising unit cell designs that have yet to be transformed into metamaterials. While it might be questioned whether the term 'unit cell' is often used outside the context of metamaterials, it is important to explore alternative search strategies that include unit cells, to uncover a broader range of options. Thus, it would be worthwhile to investigate whether including unit cells in the search parameters yields additional relevant literature. By observing the categorization it can be noticed that there is a gap in neutral stable metamaterials. There may be limited demand for neutral stable metamaterials in some applications, as other materials that exhibit positive or negative stiffness may be more suitable for certain tasks. But there is extensive literature available for neutral stable structures. So for future research on neutral stable metamaterials, one could start by reviewing neutral stable structures for unit cells.

V. CONCLUSION

The goal of this literature review is to provide an overview of different geometrically configured mechanical metamaterials with stable states, find the principles for stability and identify gaps in the literature for new research directions. An overview has been created by categorizing the literature based on their stability type and geometry, and a performance overview is provided to make comparisons between the metamaterials. Strategies were found to achieve non-linear stiffness in monostable metamaterials, multistable metamaterials, and neutral stable metamaterials. Even though many metamaterials have a single working dimension, it can be increased by making small adjustments to the unit cell and arranging it differently. Lastly, There is currently a lack of research on neutral stable metamaterials, although there is a significant amount of research on neutral stable structures. Therefore, future research can focus on exploring the properties and potential applications of neutral stable metamaterials.

REFERENCES

[1] K. Bertoldi, V. Vitelli, J. Christensen, and M. Van Hecke, "Flexible mechanical metamaterials," *Nature Reviews Materials*, vol. 2, no. 11, pp. 1–11, 2017.

[2] J. Ma, S. Chai, and Y. Chen, "Geometric design, deformation mode, and energy absorption of patterned thin-walled structures," *Mechanics of Materials*, vol. 168, p. 104269, 2022.

[3] H. Yang and L. Ma, "Multi-stable mechanical metamaterials with shape-reconfiguration and zero poisson's ratio," *Materials Design*, vol. 152, pp. 181–190, 2018.

[4] R. S. Lakes, "Negative-poisson's-ratio materials: Auxetic solids," *Annual Review of Materials Research*, vol. 47, no. 1, pp. 63–81, 2017.

[5] H. Yang and L. Ma, "1d to 3d multi-stable architected materials with zero poisson's ratio and controllable thermal expansion," *Materials Design*, vol. 188, p. 108430, 2020.

[6] H. Yang and L. Ma, "Angle-dependent transitions between structural bistability and multistability," *Advanced Engineering Materials*, vol. 22, no. 5, p. 1900871, 2020.

[7] Y. Liu, F. Pan, B. Ding, Y. Zhu, K. Yang, and Y. Chen, "Multistable shape-reconfigurable metawire in 3d space," *Extreme Mechanics Letters*, vol. 50, p. 101535, 2022.

[8] D. van der Lans, "Literature review: Strategies materials for shape morphing of compliant shells," 2021.

[9] Y. Wu, G. Guo, Z. Wei, and J. Qian, "Programming soft shape-morphing systems by harnessing strain mismatch and snap-through bistability: A review," *Materials*, vol. 15, no. 7, 2022.

[10] P. U. Kelkar, H. S. Kim, K.-H. Cho, J. Y. Kwak, C.-Y. Kang, and H.-C. Song, "Cellular auxetic structures for mechanical metamaterials: A review," *Sensors*, vol. 20, no. 11, 2020.

[11] L. Wu, Y. Wang, K. Chuang, F. Wu, Q. Wang, W. Lin, and H. Jiang, "A brief review of dynamic mechanical metamaterials for mechanical energy manipulation," *Materials Today*, vol. 44, pp. 168–193, 2021.

[12] M. A. Rifaie, H. Abdulhadi, and A. Mian, "Advances in mechanical metamaterials for vibration isolation: A review," *Advances in Mechanical Engineering*, vol. 14, no. 3, p. 16878132221082872, 2022.

[13] Z. Zhai, L. Wu, and H. Jiang, "Mechanical metamaterials based on origami and kirigami," *Applied Physics Reviews*, vol. 8, no. 4, p. 041319, 2021.

[14] Q. Lin, J. Zhou, K. Wang, D. Xu, G. Wen, Q. Wang, and C. Cai, "Low-frequency locally resonant band gap of the two-dimensional quasi-zero-stiffness metamaterials," *International Journal of Mechanical Sciences*, vol. 222, p. 107230, 2022.

[15] J. Zhou, H. Pan, C. Cai, and D. Xu, "Tunable ultralow frequency wave attenuations in one-dimensional quasi-zero-stiffness metamaterial," *International Journal of Mechanics and Materials in Design*, vol. 17, no. 2, p. 285–300, 2020.

[16] Q. Zhang, D. Guo, and G. Hu, "Tailored mechanical metamaterials with programmable quasi-zero-stiffness features for full-band vibration isolation," *Advanced Functional Materials*, vol. 31, no. 33, p. 2101428, 2021.

[17] C. Cai, J. Zhou, L. Wu, K. Wang, D. Xu, and H. Ouyang, "Design and numerical validation of quasi-zero-stiffness metamaterials for very low-frequency band gaps," *Composite Structures*, vol. 236, p. 111862, 2020.

[18] H. Fan, L. Yang, Y. Tian, and Z. Wang, "Design of metastructures with quasi-zero dynamic stiffness for vibration isolation," *Composite Structures*, vol. 243, p. 112244, 2020.

[19] A. Zolfagharian, M. Bodaghi, R. Hamzehei, L. Parr, M. Fard, and B. F. Rolfe, "3d-printed programmable mechanical metamaterials for vibration isolation and buckling control," *Sustainability*, vol. 14, no. 11, 2022.

[20] J.-X. Wang, Q.-S. Yang, Y.-L. Wei, and R. Tao, "A novel chiral metamaterial with multistability and programmable stiffness," *Smart Materials and Structures*, vol. 30, p. 065006, apr 2021.

[21] G. Wen, G. Chen, K. Long, X. Wang, J. Liu, and Y. M. Xie, "Stacked-origami mechanical metamaterial with tailored multistage stiffness," *Materials Design*, vol. 212, p. 110203, 2021.

[22] D. Karagiozova, J. Zhang, P. Chen, G. Lu, and Z. You, "Response of graded miura-ori metamaterials to quasi-static and dynamic in-plane compression," *Journal of Aerospace Engineering*, vol. 35, no. 4, p. 04022035, 2022.

[23] S. Kamrava, D. Mousanezhad, H. Ebrahimi, R. Ghosh, and A. Vaziri, "Origami-based cellular metamaterial with auxetic, bistable, and self-locking properties," *Scientific Reports*, vol. 7, p. 46046, Apr 2017.

[24] H. Ma, K. Wang, H. Zhao, R. Mu, and B. Yan, "A reusable metastructure for tri-directional energy dissipation," *International Journal of Mechanical Sciences*, vol. 214, p. 106870, 2022.

[25] X. Tan, S. Zhu, B. Wang, K. Yao, S. Chen, P. Xu, L. Wang, and Y. Sun, "Mechanical response of negative stiffness truncated-conical shell systems: experiment, numerical simulation and empirical model," *Composites Part B: Engineering*, vol. 188, p. 107898, 2020.

[26] D. Restrepo, N. D. Mankame, and P. D. Zavattieri, "Phase transforming cellular materials," *Extreme Mechanics Letters*, vol. 4, pp. 52–60, 2015.

[27] X. Tan, B. Wang, Y. Yao, K. Yao, Y. Kang, S. Zhu, S. Chen, and P. Xu, "Programmable buckling-based negative stiffness metamaterial," *Materials Letters*, vol. 262, p. 127072, 2020.

[28] H. Ma, K. Wang, H. Zhao, W. Shi, J. Xue, Y. Zhou, Q. Li, G. Wang, and B. Yan, "Energy dissipation and shock isolation using novel metamaterials," *International Journal of Mechanical Sciences*, vol. 228, p. 107464, 2022.

[29] B. Haghpanah, L. Salari-Sharif, P. Pourrajab, J. Hopkins, and L. Valdevit, "Multistable shape-reconfigurable architected materials," *Advanced Materials*, vol. 28, no. 36, pp. 7915–7920, 2016.

[30] H. Yang and L. Ma, "Angle-dependent transitions between structural bistability and multistability," *Advanced Engineering Materials*, vol. 22, no. 5, p. 1900871, 2020.

[31] H. Niknam, A. Akbarzadeh, D. Therriault, and S. Bodkhe, "Tunable thermally bistable multi-material structure," *Applied Materials Today*, vol. 28, p. 101529, 2022.

[32] H. Yang and L. Ma, "1d and 2d snapping mechanical metamaterials with cylindrical topology," *International Journal of Solids and Structures*, vol. 204-205, pp. 220–232, 2020.

[33] S. Kamrava, R. Ghosh, Z. Wang, and A. Vaziri, "Origami-inspired cellular metamaterial with anisotropic multi-stability," *Advanced Engineering Materials*, vol. 21, no. 2, p. 1800895, 2019.

[34] K. Liu, T. Tachi, and G. H. Paulino, "Bio-Inspired Origami Metamaterials With Metastable Phases Through Mechanical Phase Transitions," *Journal of Applied Mechanics*, vol. 88, 05 2021. 091002.

[35] E. Filipov and M. Redoutey, "Mechanical characteristics of the bistable origami hypar," *Extreme Mechanics Letters*, vol. 25, pp. 16–26, 2018.

[36] J. Ma, X. Jiang, and Y. Chen, "A 3d modular meta-structure with continuous mechanism motion and bistability," *Extreme Mechanics Letters*, vol. 51, p. 101584, 2022.

[37] J. Shi, H. Mofatteh, A. Mirabolghasemi, G. Desharnais, and A. Akbarzadeh, "Programmable multistable perforated shellular," *Advanced Materials*, vol. 33, no. 42, p. 2102423, 2021.

[38] T. Mukhopadhyay, J. Ma, H. Feng, D. Hou, J. M. Gattas, Y. Chen, and Z. You, "Programmable stiffness and shape modulation in origami materials: Emergence of a distant actuation feature," *Applied Materials Today*, vol. 19, p. 100537, 2020.

3

Research paper

Towards a neutrally stable compressible metamaterial

Jeffrey Zhu, Giuseppe Radaelli

Department of Precision and Microsystems Engineering, Faculty of Mechanical Engineering and Marine Technology, Delft University of Technology, The Netherlands

***Abstract*—Neutrally stable metamaterials can maintain different shapes without any energy input, making it a key innovation in the quest for more energy-efficient technologies. Despite this intriguing property, the research in this area is scarce. This study proposes a method for achieving neutral stability in metamaterials. This method is validated with a novel unit cell design that utilizing two identical beam elements that are mirrored. Each element displays a constant force characteristic. By pretensioning these elements, we align their constant force regions, thereby inducing a state of neutral stability. Through finite element method (FEM) simulations and geometrical optimisation, the beam of this design is optimised to achieve the optimal constant force response. A prototype is made and a test setup is constructed to validate the accuracy of the simulations and the feasibility of the method for achieving neutral stability. Results indicate that while perfect neutral stability was not fully achieved, this method can be applied on other constant force mechanisms to create neutrally stable metamaterials.**

I. Introduction

Metamaterials have attracted much attention in the last two decades due to their ability to possess unusual properties [1]. Their extraordinary properties are derived not from the materials they are made of but from their precisely designed geometric structures [2] [3]. This gives metamaterials the ability to possess properties that are unusual and extreme compared to constituent materials.

Mechanical metamaterials are a subgroup of metamaterials that focus on motion, displacements, stresses, and mechanical energy [4]. For example, they can display negative stiffness behaviors [5] [6], where the material compresses under tensile stress and expands under compressive stress, defying conventional material responses. Additionally, they can exhibit negative thermal expansion [7], contracting when heated rather than expanding as traditional materials do. Furthermore, the Poisson's ratio in these materials can be tailored to be positive, zero, or negative [7] [8] [9], allowing for expansion, neutral response, or contraction perpendicular to an applied force, respectively.

Mechanical metamaterials with nonlinear stiffness properties are captivating for their stiffness programmability [10], their potential in energy absorption applications [11], and their shape-morphing capabilities [12]. These nonlinear stiffness metamaterials can be classified into three types of stability, namely monostability, multistability, and neutral stability.

Monostable nonlinear stiffness metamaterials include metamaterials with constant force properties, also called Quasi-zero stiffness properties. This refers to metamaterials with a single minimum in their potential energy landscape. The corresponding stiffness characteristic is high stiffness transitioning to almost zero stiffness as the displacement increases to a certain level. A possible application for these metamaterials is vibration isolation [13] [14].

Conversely, metamaterials with multistability introduce a framework where multiple equilibrium states are feasible, caused by the presence of multiple local minima within their potential energy landscape. This is typically achieved through the tessellation of bistable unit cells. The unit cells often consist of some variation of a beam with two equilibrium positions. These types of metamaterials could be used for energy absorption [15] [16] and shape morphing [17].

On the other hand, neutral stability in metamaterials is also an intriguing feature. In theory, these structures maintain a constant potential energy across the energy landscape, indicating that they do not require a force to deform or remain deformed. Their ability to change and sustain different shapes without requiring energy makes them an important innovation in developing more energy-efficient technology. For example, in linear guidance systems, mechanisms with zero stiffness in one direction (the guiding direction) but high stiffness in others are required. Neutrally stable metamaterials could meet this requirement. Despite the intriguing nature of neutrally stable metamaterials, research in this area is noticeably scarce. Research by Mukhopadhyay et al. [18] showcases an origami-based tubular-shaped metamaterial. This metamaterial is based on a waterbomb crease pattern and can exhibit negative stiffness properties and near-neutral stability by changing the tesselation sequence and folding angle. Additionally, research by Cai et al. [19] designed a novel one-dimensional quasi-zero stiffness metamaterial. The unit cell of this metamaterial is made of an elastic positive stiffness element and two buckling beams with negative stiffness elements. The positive stiffness can be neutralized by the negative stiffness, leading to the quasi-zero stiffness behavior. Near-neutral stability can be achieved in the unit cell by applying a pre-load. However, the neutral stable behavior is within the boundaries of the unit cell, thus the displacement region of neutral stability will not increase for the metamaterial. All in all, in the current research, no general method was found for creating neutrally stable metamaterials.

This paper presents a novel method for achieving neutral stability in metamaterials. It proposes a novel unit cell design with constant force properties. This unit cell consists of an upper half and a lower half. The upper half is the mirrored version of the lower half, both made up of four spline-shaped beams that are designed to experience lateral torsional buckling (LTB), inducing a constant force behavior. By introducing pre-tension in both the upper and lower halves of the unit cell, the areas exhibiting constant force characteristics are aligned with one another. This alignment shifts the behavior from a constant force response to a zero-force state, thereby achieving a neutrally stable behavior.

The primary goal of this paper is to assess the feasibility of this approach for achieving neutral stability. To accomplish this, the unit cell is geometrically optimized and then subjected to tests that mimic the expected behavior of the metamaterial. The subsequent analysis of the force-displacement results from these tests serves as the foundation for determining the method's viability.

This paper is structured as follows: in section II, the concept of the design and working principle will be explained. The corresponding finite element method (FEM) model and the optimization model will also be discussed. Afterward, the prototype fabrication and the test setup are elaborated upon. The experimental results of the constant force unit cell and the pre-tensioned unit cell will be shown in section III. In section IV, the results are analyzed, and ideas for future improvements and recommendations are presented. Finally, the conclusion and contributions will be summarized in section V.

II. Method

The process of making and evaluating the unit cell in the metamaterial consists of different aspects. These aspects are discussed in the following subsections. The overall procedure can be summarized as follows: (1) A numerical model was made to predict the behavior of the metamaterial. (2) The final geometry was derived from an optimisation consisting of different beam parameters. (3) The unit cells were produced and (4) tested under boundary conditions that correspond to the behavior of a metamaterial.

A. Concept

The core idea of the unit cell's design revolves around employing two identical elements that exert a constant force and arranging them such that their forces neutralize each other, resulting in a neutrally stable behavior. In this design, the identical elements are mirrored and then pre-tensioned. Pre-tensioning is required to align the constant force regions with each other. The force-displacement behavior and the influence of pre-tension are shown in Figure 1.

There are two variants of this unit cell design, namely a simplified 2D variant of the unit cell mainly used for the experiments and a 3D unit cell used for the construction of the metamaterial. The 2D unit cell consists of a top part and a mirrored bottom part. Both the top and bottom parts, consisting of two B-spline curved beams, exhibit constant force behavior. In Figure 2 the top part consists of two beams referred to as beam set 1 and the beams of the bottom part are referred to as beam set 2. Figure 2 also shows the 2D unit cell in the state where it is not pre-tensioned, the state where pre-tension is applied, and the state where it is pre-tensioned and a displacement is applied.

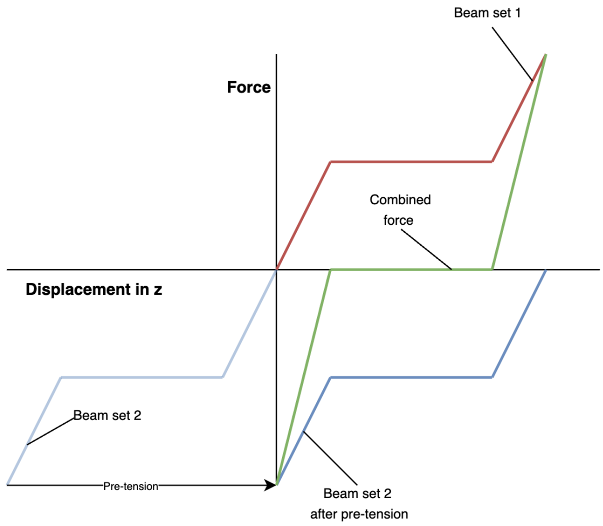

Fig. 1. Visualisation of constant force element 1 (red), mirrored element (light blue), mirrored and pre-tensioned element (dark blue), and the resulting zero force when combined (green).

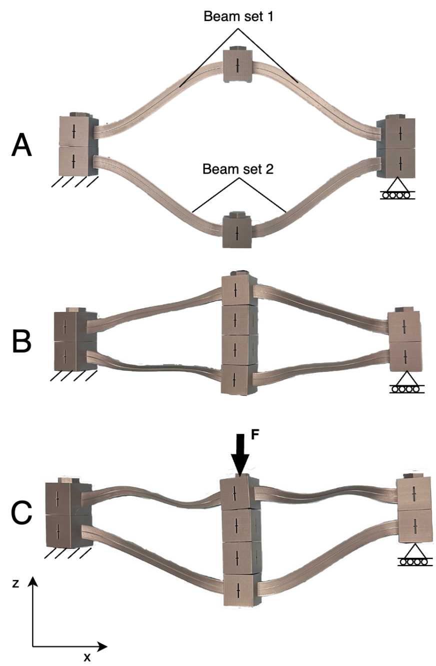

Fig. 2. 2D schematic view of unit cell with pre-tension and deformation sequence. A) shows the unit cell in neutral position. B) shows the unit cell in pre-tensioned state. C) shows the deformed pre-tensioned unit cell. The response of the applied force corresponds to the 'combined force' behavior.

The proposed 3D unit cell of the metamaterial consists of eight B-spline curved beams. The unit cell can be split into an upper and lower part, either consisting of four beams connected at a 90-degree angle, as can be seen from the top view in Figure 3. This design contrasts with the 2D unit cell, where the top and bottom parts are formed by two beams joined at a 180-degree angle. Figure 3 shows the 3D outline of the unit cell without dimensions and cross-sectional area of the beams. The unit cell is also symmetric in the xy-, xz-, and yz-planes.

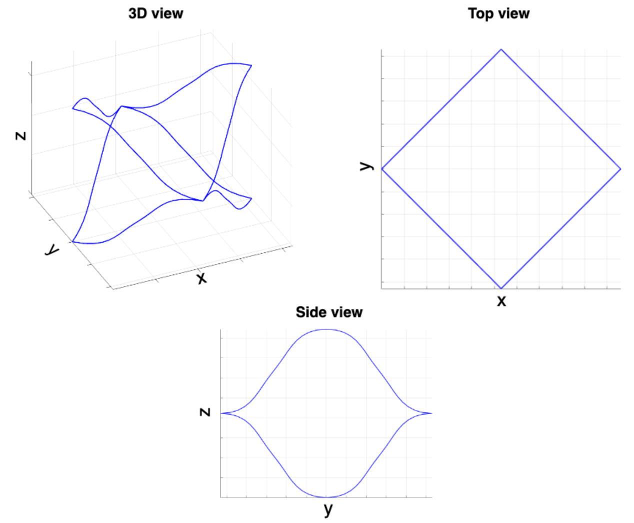

Fig. 3. Outline of the unit cell shown in three different perspectives.

Finally, the unit cells are tessellated to form the metamaterial. The top and side views of a 3x3x5 metamaterial can be seen in Figure 4. The side views show how the unit cells are tessellated in height. As can be seen in the undeformed side view, the output junction of one unit cell is connected to the input junction of the unit cell underneath. The output passes a displacement along to the input, such that the displacement range of the metamaterial is proportional to the number of rows.

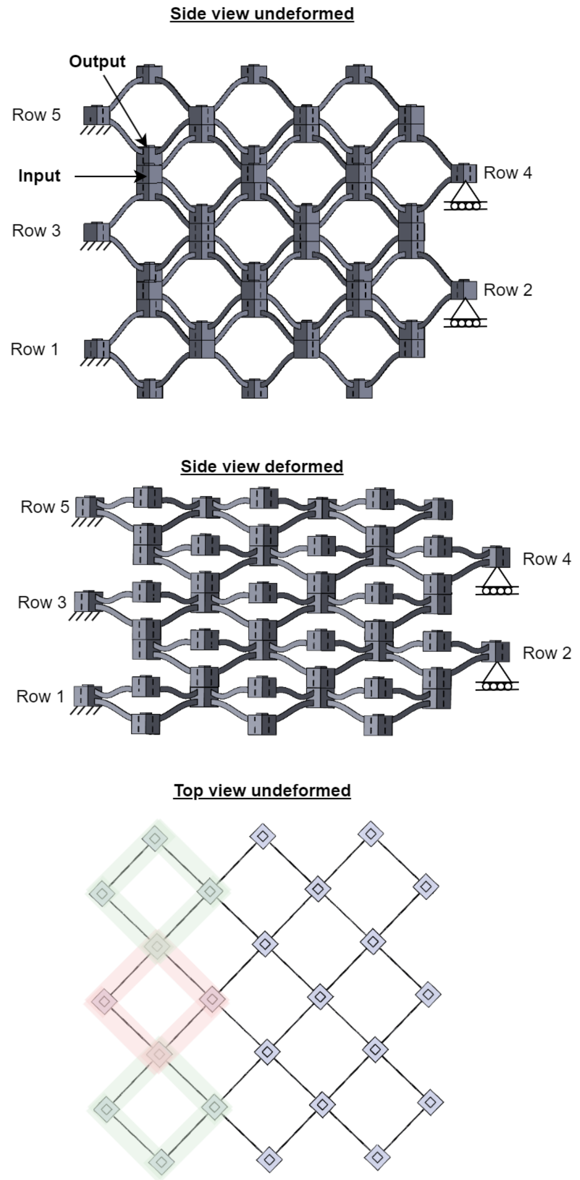

Fig. 4. The undeformed and deformed side view and the top view of the metamaterial consisting of 3x3x5 tessellated unit cells. The input junction is connected to the output junction so that the displacements of the rows can be passed along to the other rows. Three unit cells are highlighted in the top view to show how the unit cells are tessellated.

B. FEM model

The simulations are performed using a three-dimensional beam model with a custom finite element method (FEM) model. This solver is based on geometrically non-linear and co-rotational beam elements using the Euler-Bernoulli beam formulation proposed by Battini [20]. The beam model creates a beam structure based on a set of nodes. Each node has its own user-defined locations, nodal mechanical material properties (youngs modulus E, shear modulus G), and nodal cross-sectional properties (area moment of inertias I_{yy}, I_{zz} and torsional constant J). The computation of the deformation is based on the nodal properties. Application of forces and displacements is simulated through the custom FEM solver.

A cruciform was selected as the cross-section for the beam. A cruciform cross-section can exhibit lateral torsional buckling, inducing constant force behavior. Besides, the area moment of inertia and torsional constant can span a wide range of values by changing the geometrical parameters. The cruciform is defined with the parameters t_v, H_v, t_h, and W_h as depicted in Figure 5.

The area moment of inertias is derived using the following formulas:

$$I_{yy} = \int z^2 dA \tag{1}$$

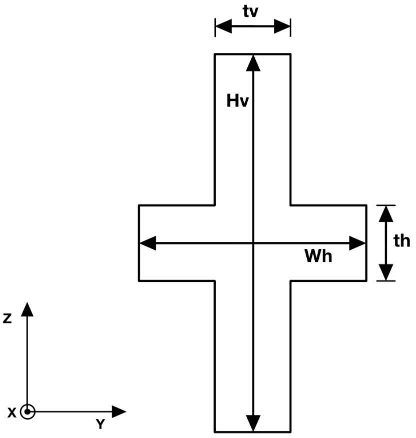

Fig. 5. Cruciform cross-section defined with parameters H_v, t_v, W_h and, t_h.

and

$$I_{zz} = \int y^2 dA \tag{2}$$

The torsional constant for open cross-sections can be approximated by breaking the sections down into rectangles with sides b and t, where t<b. The following formulation by Timoshenko [21] can then be used:

$$J = \sum(\frac{bt}{3} - \frac{t^4}{5}) \tag{3}$$

Periodic boundary conditions (PBCs) were used to simulate the metamaterial behavior efficiently. PBCs are a mathematical construct applied in simulations to model a small part of a material while representing the behavior of an infinite system, in this case the unit cell and metamaterial, respectively. The PBCs method simulates the unit cell as an endless metamaterial by ensuring that every pair of opposite boundaries undergo identical deformations. This creates a condition where influences from the edges or boundaries are entirely removed, effectively replicating an infinite system where the central repeating unit's behavior is isolated from external constraints [22].

NURBS an acronym for Non-Uniform Rational B-Splines, were adopted as the shape for the beams. Initially, the beams were designed to be straight, which worked for individual unit cells. However, significant stress concentrations were observed at the junctions. NURBS was implemented as a replacement for the straight beams to avoid this issue. Figure 6 visualizes the principle for defining the NURBS coefficients.

The NURBS is constructed using the NURBS Toolbox by D.M. Sprink [23] on Matlab. C4 is the midpoint and lies at the intersection of the horizontal and vertical axes. To derive the coefficients C5, C6, and C7, start by reflecting C1, C2, and C3 about the vertical axis, followed by a reflection about the horizontal axis. The y coordinates of C1 and C2 are identical, a pattern also observed between C6 and C7. This way, the stresses at the junction will be reduced. C3 and C5 are equal in magnitude with respect to C4 but located in different

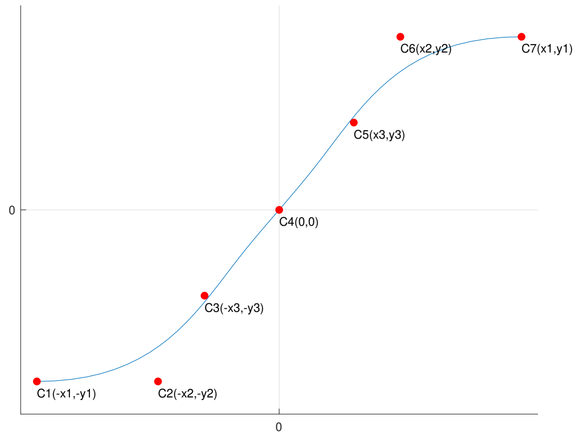

Fig. 6. Visualisation of the relative positions between NURBS coefficients. C1 & C7, C2 & C6, and C3 & C5 have the same magnitude but are positioned in different quadrants.

quadrants. The following non-decreasing knot sequence was used for the creation of the NURBS: [0 0 0 0 0.4 0.5 0.6 1 1 1 1]. The coefficients used for the construction of Nurbs are shown in Table I. Note that the final NURBS shape is calibrated such that C1 is on the origin instead of C4. The principle remains the same.

TABLE I
COEFFICIENTS USED FOR THE FINAL NURBS SHAPE

Coefficient	X and Y coordinates (in mm)
C1	X=0, Y=0
C2	X=0, Y=37.5
C3	X=51.9, Y=21
C4	X=75, Y=42
C5	X=98.1, Y=63.375
C6	X=112.5, Y=84.375
C7	X=150, Y=84.375

The material properties were also required for the simulation. Polyactic acid (PLA) was used as the material for the simulation. The corresponding value for Young's modulus was E =3.5 GPa, and the shear modulus was G =1.1 GPa [24].

C. Geometric optimisation

The cross-section geometry was optimized using Matlab. The 'fmincon' function from Matlab's optimisation toolbox was used for this task. The advantage of using 'fmincon' is that it allows the user to set specific upper and lower bounds for the parameters being optimized. This feature was necessary to avoid unrealistic solutions. The parameters H_v and W_h were established with lower and upper limits of 1e-4 m, and 20e-3 m, respectively. The parameters t_v and t_h were bounded between 0.1e-3 m and 1.5e-3 m.

Fmincon searches for solutions that reduce the objective function until it finds a local minimum. In this case, we are looking for a force-displacement behavior that exhibits constant force behavior. A mean squared error (MSE) equation was used to convert the desired behavior into an objective function. The objective function is designed to calculate the squared relative error between a measured force (F) value and the mean force (F_m), averaged over all measured values. The MSE equation is described as follows:

$$\sum\left(\frac{F - F_m}{F_m}\right)^2 \tag{4}$$

The objective function focused solely on the last 70% of displacement, leaving out the first 30%. This approach comes from the goal of maximizing the displacement range over which the force remains constant. The initial displacement segment was excluded because it is considered the settling phase, which the system needs to approach the constant force phase.

D. Prototype fabrication

It was not possible to 3D print the unit cell monolithically, so the prototype building process was divided into several parts. The unit cell consists of beams that are connected to one another. So firstly, the beams were printed as two halves and bonded together with Loctite super glue. The beams are then connected with a block with a geometric cutout matching the cross-section of the beams. The tolerance was set such that the beams could be tightly fitted and not slip out. The design of the connecting block is shown in Figure 7. The beams and connecting blocks are connected to each other to form the full unit cell and metamaterial. The complete 3D unit cell prototype is shown in Figure 8.

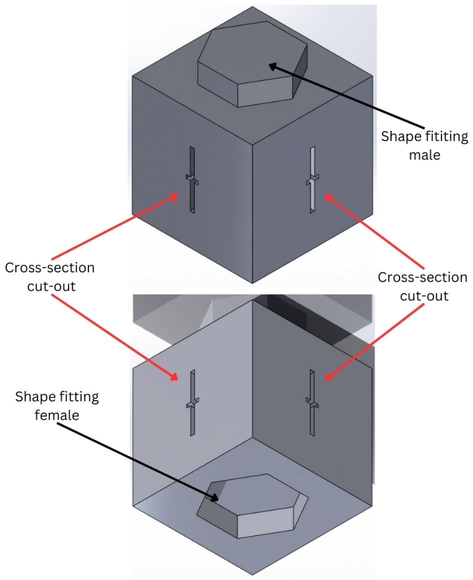

Fig. 7. Top isometric view of the connecting block (top). Bottom isometric view of the connecting block (bottom).

Fused deposition modeling 3D printing was a suitable option for fabricating the physical model due to its ability to make complex shapes. The prototypes are all printed using the original Prusa i3 MK3S+ 3D printer. The default bed is interchanged with a flexible bed, such that the prints can be removed easily afterward. For the filament, PLA from the brand REAL is used. All CAD files were made in Solidworks, and the corresponding g-codes were generated in PrusaSlicer. An infill density of 100% was used for the beams and 15% was used for the blocks, with a gyroid infill pattern. More information about the dimensions of the block can be found in Appendix A.

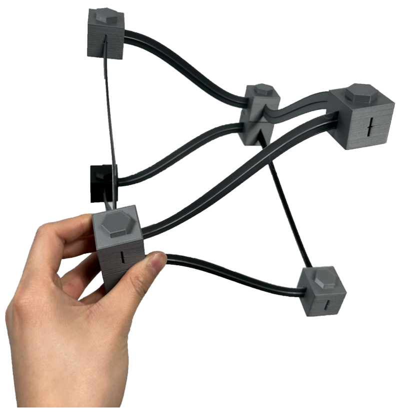

Fig. 8. Complete prototype of the 3D unit cell.

E. Experimental setup

To validate the accuracy of the simulations and the method used to establish neutral stability, an experimental setup was designed. This setup involved testing both individual beam sets and the entire 2D unit cell. Firstly, beam set 1 and beam set 2 are tested on their constant force behavior. A comparison will then be made between the experimental results and the FEM simulation results to validate the simulations. This setup is shown in Figure 9

Subsequently, the pre-tensioned 2D unit cell will be tested. Tests will be conducted on various levels of pre-tension. As seen in Figure 1 the force-displacement responses will shift when a pre-tension is applied. These experiments aim to validate whether adjusting the constant force regions through pre-tension effectively achieves neutral stability. This 2D unit cell's experimental setup is shown in Figure 10. The experimental results will be compared to the FEM simulation results. Also, the experimental results of beam set 1 will be manually combined by mirroring and shifting the force-displacement response the same way as shown in Figure 1. This is done to get a more accurate approximation of the behavior of the physical pre-tensioned 2D unit cell. This approximation will also be compared to the experimental results of the 2D unit cell.

The setup consists of two rails made from Thorlabs 25x25mm profiles. A rail guide was attached to each rail, providing one degree of freedom (DOF) in the x-direction, as seen in Figure 9. The rail guide was made of a V-slot profile guided by three V-slot wheels and the lower part of the beam sets is connected to the V-slot profile with a steel axis. A hole

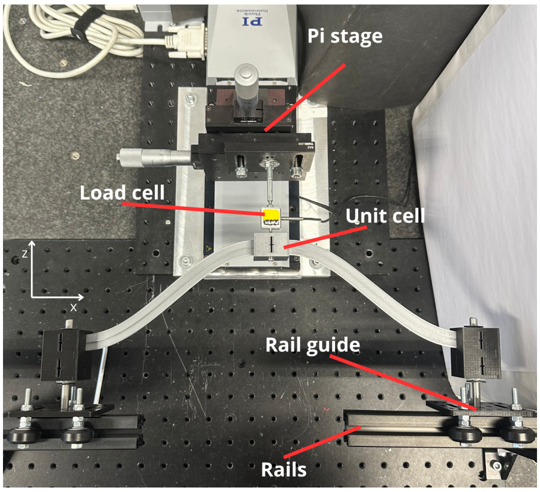

Fig. 9. Top view of half a unit cell experimental setup.

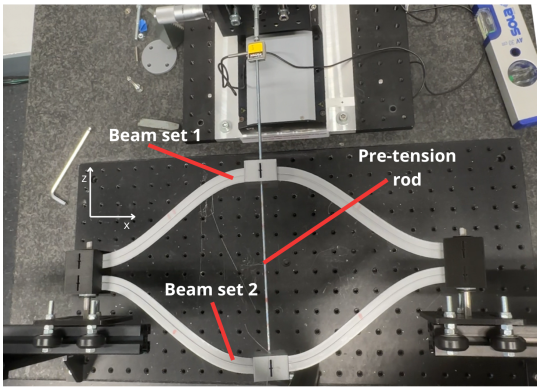

Fig. 10. Top view of complete unit cell experimental setup. Beam set 1 and beam set 2 are pre-tensioned with the pre-tension rod. The rod is made from a screw thread such that the distance between the two beam sets can be adjusted accordingly.

was made in the geometric cutout block such that the axis could fit through the block with a ball bearing allowing only one rotational DOF around the Z-axis. More on the dimensions and design of the rail guide can be found in Appendix A. The top part of the beam sets is connected to the Futek FSH03875 load cell to measure the reaction forces, with a force limit of 45 N. Finally, the load cell is connected to the M-505.4DG PI stage. The PI stage can realize a maximum translation of 100 mm, which is used to compress and extend the unit cell.

The experimental setup for the 2D unit cell is a little different. To apply pre-tension the two opposing blocks of the beam sets are connected by screwing a screw thread through the center of the blocks. The pre-tension can be manually adjusted by adjusting the distance between the two blocks. The force-displacement behavior of the pre-tensioned 2D unit cell is tested with pre-tension levels of 40 mm, 60 mm, 80 mm, 100 mm, 120 mm, and 140 mm. A pre-tension of 40 mm means that the distance between the two blocks was reduced by 40 mm from the equilibrium distance, so in principle, each beam set of the 2D unit cell is pre-tensioned by 20 mm.

III. Results

The results section is divided into several parts. First, the results of the force-displacement behavior of the optimized beam sets will be compared to the experimental results to validate the constant force behavior. Subsequently, the results of the 2D pre-tensioned unit cell will be shown.

A. *Constant force*

The results of the geometric optimisation discussed in subsection II-C is shown in Table II. One prototyped beam of beams set 1 is measured for comparison and the measured values are also displayed in Table II.

TABLE II
Optimised parameter values and the measured values

Geometry parameter	Optimised value in(m)	Measured value in(m)
Hv	13.3×10^{-3}	13.5×10^{-3}
tv	0.786×10^{-3}	0.85×10^{-3}
Wh	2.77×10^{-3}	2.85×10^{-3}
th	0.566×10^{-3}	0.65×10^{-3}

Experiments were conducted on the two beam sets. A displacement of 70 mm was applied to each beam set. In Figure 11 the grey area corresponds to the hysteresis result of the experiment. The elastic response of the experimental results is addressed with dashed lines. The elastic response is the mean of the hysteresis area. Furthermore, the overall shape of the two beam sets is similar, showing high stiffness from 0 to 20 mm and a reduced stiffness profile from 20 mm to around 50 mm. However, the two beam sets do show a discrepancy in the magnitude of their force profiles.

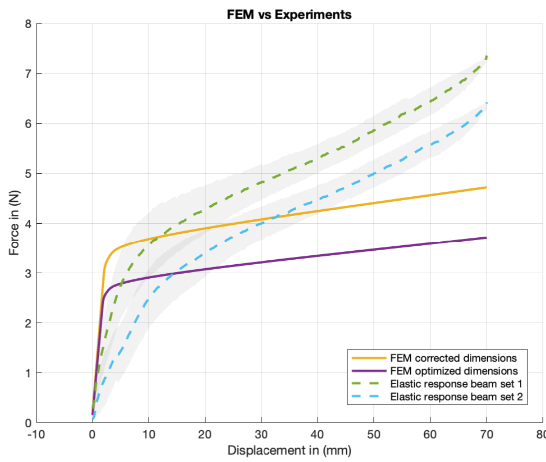

Fig. 11. Experimental results of the beam sets (dashed lines) compared to the simulation results (solid lines).

Figure 11 also shows a comparison of the experimental results with the simulation results. The purple line represents the results of the simulation with optimized cross-sectional dimensions. The blue line also represents the results of the simulations but with the corrected dimensions.

A few things can be noticed when comparing the experimental and simulation results. First of all, the settling distance for reaching the reduced stiffness is nearly zero for the simulation results. Secondly, the reduced stiffness of the simulation results is lower than the reduced stiffness of the experiments. Finally, while both results show a reduction in stiffness, none show a perfect zero stiffness area.

B. Neutral stability

The results of the influence of pre-tension are shown in three different ways. Firstly, the results of the optimal case are shown in Figure 12 depicted with solid lines. These results are extracted from the FEM simulation by manually combining the results of the two optimized single beams using the method explained in subsection II-A.

Secondly, the experimental data from beam set 1 is also manually combined to analyze the theoretical results when two beams identical to beam set 1 are pre-tensioned. These results are capped at a pre-tension of 100 mm, constrained by the absence of comprehensive experimental data. These results are shown in Figure 12 depicted with dashed lines.

In both results, it can be noticed that with increasing pre-tension, the stiffness remains lower for longer displacements. Also, the reduced stiffness area for the combined beam set 1 case is larger than the optimal case.

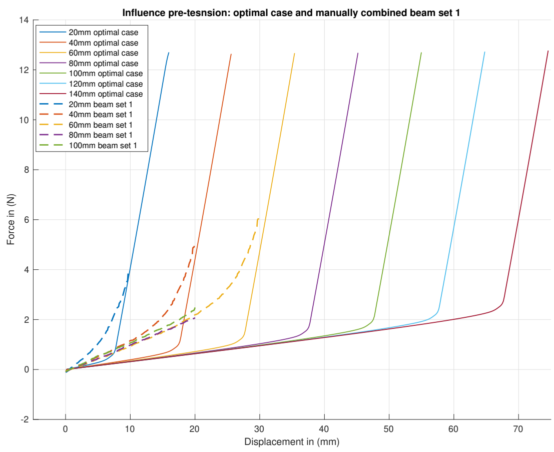

Fig. 12. Influence of pre-tension for the optimal case and the case of manually combined beam set 1. The solid lines correspond to the optimal case and the dashed lines correspond to the case of beam set 1.

Lastly, the experimental results validating the method for achieving neutral stability are shown in Figure 13. Experiments with different pre-tensions ranging from 40 to 120 mm were conducted on the 2D unit cell. The results show the elastic responses derived from the hysteresis mean. It can be seen that applying a pre-tension of 40 and 60 mm to the 2D unit cell increases the stiffness, while a pre-tension of 80 to 140 mm reduces the stiffness. Another noticeable thing is that the 80 to 140 mm pre-tensioned unit cell responses are clustered together.

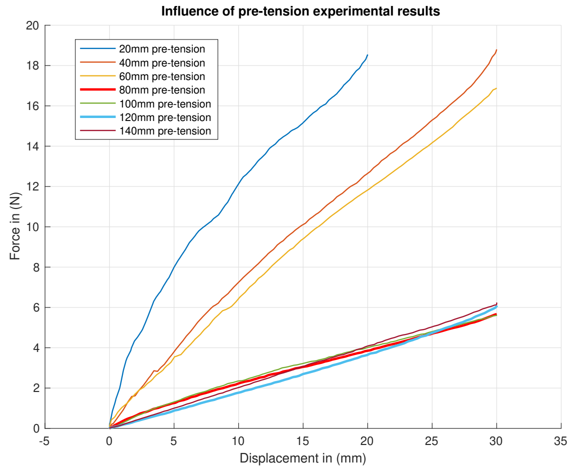

Fig. 13. Experimental results of the 2D unit cell with increasing pre-tensions.

IV. Discussion

A. Constant force

In Figure 11 a magnitude difference can be noticed between the two beam sets. Several factors may cause this difference. First of all, prototyping irregularities. The beams are 3D printed and have feature sizes in the order of sub-millimeters. Even though measurements were made to reduce the error by decreasing the layer height and printing speed for more accuracy, errors still occurred. Examples of errors are uneven surfaces and differences in dimensions. Besides irregularities in the 3D printing, imperfections also occurred in the gluing part. This resulted in the cruciform cross-section not being entirely aligned and symmetrical. Cumulatively, these imperfections could impact both the magnitude and general behavior of the beams. The impact of enlarging the cross-section by 0.1 mm, 0.3 mm, and 0.5mm beyond the optimized dimensions is depicted in Figure 14. Notably, there is a significant increase in magnitude correlating with the increase in error size. Additionally, when the error reaches 0.5 mm, there is also an observable increase in the stiffness of the section with reduced stiffness.

The experimental results also showed some discrepancies compared to the simulation as shown in Figure 11. Firstly, the settling distance for the beam to reach the reduced stiffness area is very small in the simulation case. This can be explained by the fact that the simulations are run in perfect conditions, meaning there are no imperfections in the material. This makes the simulation not deform laterally, but rather no deformation happens until it reaches a certain bifurcation point where it instantly snaps into post-buckling mode, while in real life

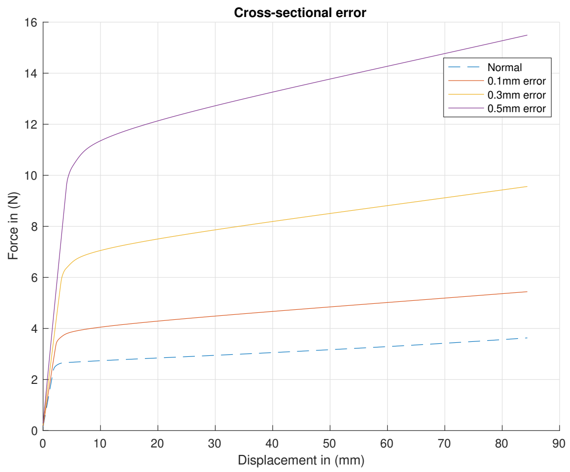

Fig. 14. Effect of a larger cross-section. Every parameter of the cross-section is enlarged with 0.1mm, 0.3mm, and 0.5mm.

this buckling happens less abruptly. This phenomenon can be illustrated by an axially compressed bar. When the load is not far away from the buckling load, an imperfection in the bar or a small eccentricity of the loading will bend the bar significantly. While in perfect condition, the bar will remain straight [25]. In the simulation, imperfections can be added to the geometry. In this case, the imperfection is added as a small random displacement to the nodes in the x- and y-directions. In Figure 15 a response with imperfections in the geometry is compared with the response of the ideal geometry. As can be noticed, the imperfections increase the settling distance, and the transition from high stiffness to reduced stiffness is more gradual.

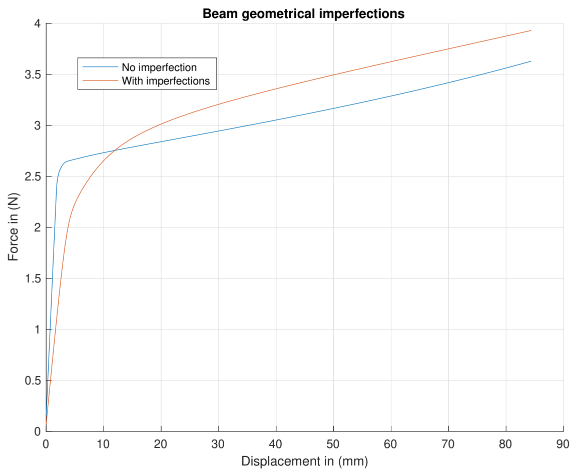

Fig. 15. Effect of adding geometrical imperfections.

Despite using the known Young's modulus and shear modulus values of PLA for the simulations, these may not be entirely accurate reflections of the material properties. The 3D printing process used to create the physical components significantly influences these moduli. Factors such as the orientation of printing and the direction of load application play a crucial role in determining the 'real' moduli. The strength of the parts is greater in directions parallel to the printing direction and weaker in perpendicular directions. Additionally, the bonding strength of the super glue used in assembly can also affect the 'real' moduli of the parts.

Figure 16 and Figure 17 present simulation results with varying moduli. In Figure 16, while the Young's modulus is altered, the shear modulus is held constant, and the reverse is true for Figure 17. Both figures illustrate that the changes in moduli only affect the magnitude, while the settling distance and stiffness of the models remain unchanged.

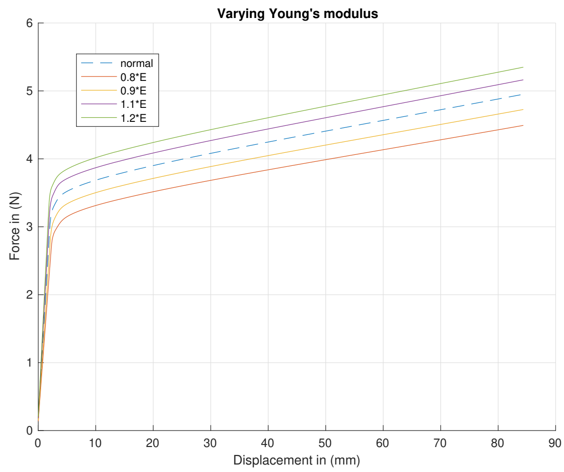

Fig. 16. Variation of Young's modulus compared to the used Young's modulus. With values 20% lower to 20% higher than the used Young's modulus.

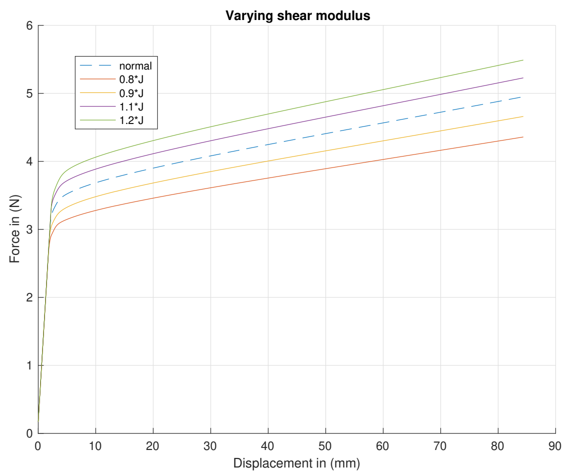

Fig. 17. Variation of Shear modulus compared to the used Shear modulus. With values 20% lower to 20% higher than the used Shear modulus.

Furthermore, a remark can be made about the FEM method. The simulations employed an Euler-beam model, which might not be the most suitable choice considering the optimized cross-section's thin features. A shell model could potentially offer more accuracy in this context. This is because an Euler-beam model operates under the assumption that the cross-section stays flat and perpendicular to the neutral axis post-deformation, and keeps its in-plane shape. However, this assumption does not hold for shell structures.

In conclusion, by accounting for the cumulative errors of an imperfect geometry, a cross-section enlarged by 0.3 mm, and a 10% decrease in Young's modulus, the response aligns more closely with experimental observations, as depicted in Figure 18. Notably, the settling distance is further increased compared to when the geometric imperfection is considered in isolation from other errors.

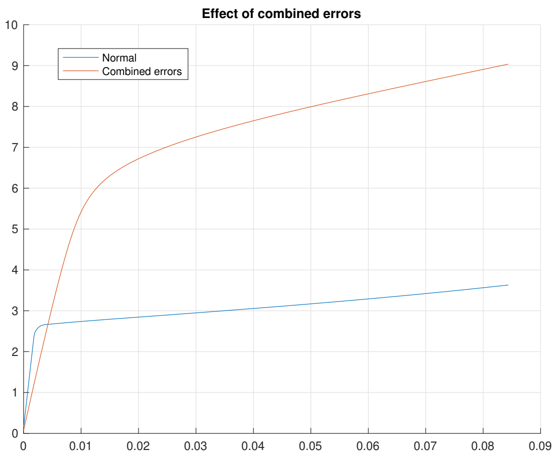

Fig. 18. Effect of combining an imperfect beam geometry, 0.3mm larger cross-section, and a 10% reduction in Young's modulus compared to the perfectly optimised response (normal).

B. *Neutral stability*

In examining how pre-tension affects both the optimal case and the combined beam set 1 case, various distinctions are noticeable from Figure 12. The singly optimized beam exhibits a notably brief yet sharp settling distance and an almost flat area of reduced stiffness. When two such beams are coupled and pre-tensioned, this results in an area that more closely approaches a near-zero force profile. This contrasts with combining beam set 1, which requires a larger pre-tension to reach the near-zero force profile. Moreover, in the case of the combined beam set 1, the achieved near-zero force profile is less close to actual zero force compared to the combined, pre-tensioned optimized beams. This can be explained by the fact that the reduced stiffness area of beam set 1 is larger than the reduced stiffness area of the optimized beam set.

There are two main discrepancies between the experimental data and the approximation from the manually combined data of beam set 1. The first one is the force profile. The expected behavior is that the slope of the force profile increases after a certain displacement. For example, in the case of 20 mm pre-tension, the slope was expected to increase after 10 mm, but this behavior can not be observed in the experimental data. Furthermore, the secant stiffnesses from the experimental results and approximated results were evaluated. The secant stiffness for a pre-tension of 20 mm was evaluated at 10 mm displacement. The other secant stiffnesses are evaluated at 20 mm displacement. The results are shown in Table III. It can be noticed that there is a factor difference between the secant stiffness of the approximation and the experiment. The factor difference decreases with the increase of the pre-tension. These discrepancies could be caused by the method of connecting the beams. These discrepancies could potentially be attributed to the method used for connecting the beams, suggesting that the connection technique might have influenced the structural behavior. While the exact causes of these discrepancies are not currently understood, they point to areas for further investigation.

TABLE III
SECANT STIFFNESS

Pre-tension	**Secant stiffness from approximation**	**Secant stiffness from experiment**
20 mm	$k \approx 0.39\ N/mm$	$k \approx 1.2\ N/mm$
40 mm	$k \approx 0.25\ N/mm$	$k \approx 0.63\ N/mm$
60 mm	$k \approx 0.11\ N/mm$	$k \approx 0.58\ N/mm$
80 to 120 mm	$k \approx 0.11\ N/mm$	$k \approx 0.2\ N/mm$

The experimental data detailed in Figure 13 demonstrate that pre-tensioning successfully lowers the stiffness of the unit cell. Even though the overall shape differs from the expected results, the experimental results do show that by adding pre-tension the stiffness reduces. So by adding energy to the system, less energy is required to make the same displacement.

Although the goal of neutral stability was not fully realized, these results validate the method's effectiveness. The inability to achieve neutral stability can be attributed to the beam sets not exhibiting constant force behavior. Consequently, this led to the absence of regions with zero stiffness, thereby eliminating the potential for neutralizing the forces. This novel approach to achieving neutral stability relies on the constant force behavior of the beam sets. If this behavior were perfected, the unit cell would likely attain neutral stability. Therefore, this method opens up possibilities for employing other designs that exhibit constant force characteristics to achieve similar outcomes.

C. *Future research*

For future research, several improvements can be made regarding the design and manufacturability. A primary goal is to refine the force response, as neither FEM simulations nor experimental outcomes currently exhibit the ideal constant force response necessary for achieving neutral stability. This objective might be accomplished by exploring alternative designs, including experimenting with different cross-sectional shapes capable of exhibiting LTB behavior. An I-shaped cross-section, for example, may offer a more consistent force response. Additionally, investigating the impact of varying B-spline shapes combined with the new cross-section may also provide valuable insight. Another area of potential improvement involves examining the effects of altering the cross-section orientation. Currently, the local coordinate systems at each node of the beam are uniform. Changing this may lead to improvements.

In terms of manufacturability, it is worth exploring alternative prototyping techniques to make the prototype more accurate. Nevertheless, given the complexity of the design, 3D printing likely remains the most feasible method for creating prototypes. The current flaws mainly come from the relatively small feature sizes. Additionally, creating the prototype as a single, monolithic piece would more closely align with the outcomes predicted by FEM simulations while also significantly reducing prototyping time. Also, the current method for pre-tensioning is not optimal. A design change should be made such that the whole metamaterial can be pre-tensioned in one motion.

This research primarily focuses on the behavior of a single unit cell under periodic boundary conditions, aiming to replicate the overall behavior of the metamaterial. However, the impact of the tessellation sequence on the metamaterial's properties remains uncertain. Addressing this uncertainty requires either constructing a smaller-scale prototype or using a larger test setup. This step is crucial for a deeper understanding and effective application of the metamaterial in practical scenarios.

Lastly, while investigating the deformations of the unit cell it seemed that the beams could buckle in two directions when being compressed. This behavior allows the metamaterial to have a sign-switching Poisson's ratio which does not exist in constituent materials. This can also be further investigated. More on the sign switching Poisson's ratio behavior of this metamaterial can be found in Appendix D.

V. Conclusion

This study presents a novel method for creating neutral stability in metamaterials. This is done by employing two identical elements that possess constant force-displacement behavior. These two elements are mirrored and pre-tensioned such that the constant force regions align and result in a constant zero force region, creating neutral stability.

A beam cross-section optimisation was conducted to find the optimal cross-section for the best constant force performance. The optimized solutions showed nearly constant force behavior but not a perfect one.

Prototypes were made and experimentally tested to validate this method of creating neutral stability. Discrepancies were observed between the simulations and the experimental results, which can be partially explained by manufacturing uncertainties. Even though perfect neutral stability was not achieved, the experiments proved that the method could work if a perfect constant force element could be manufactured.

The results give confidence that this method can be applied to other constant force mechanisms to create neutrally stable metamaterials.

References

[1] P. Jiao, J. Mueller, J. R. Raney, X. R. Zheng, and A. H. Alavi, "Mechanical metamaterials and beyond," *Nature Communications*, vol. 14, p. 6004, Sep 2023.

[2] J. U. Surjadi, L. Gao, H. Du, X. Li, X. Xiong, N. X. Fang, and Y. Lu, "Mechanical metamaterials and their engineering applications," *Advanced Engineering Materials*, vol. 21, no. 3, p. 1800864, 2019.

[3] L. Wu, Y. Wang, K. Chuang, F. Wu, Q. Wang, W. Lin, and H. Jiang, "A brief review of dynamic mechanical metamaterials for mechanical energy manipulation," *Materials Today*, vol. 44, pp. 168–193, 2021.

[4] K. Bertoldi, V. Vitelli, J. Christensen, and M. van Hecke, "Flexible mechanical metamaterials," *Nature Reviews Materials*, vol. 2, p. 17066, Oct 2017.

[5] R. Lakes, T. Lee, A. Bersie, and Y. Wang, "Extreme damping in composite materials with negative-stiffness inclusions," *Nature*, vol. 410, no. 6828, p. 565 – 567, 2001.

[6] H. Ma, K. Wang, H. Zhao, R. Mu, and B. Yan, "A reusable metastructure for tri-directional energy dissipation," *International Journal of Mechanical Sciences*, vol. 214, p. 106870, Jan 2022.

[7] H. Yang and L. Ma, "Angle-dependent transitions between structural bistability and multistability," *Advanced Engineering Materials*, vol. 22, no. 5, p. 1900871, 2020.

[8] K. Bertoldi, P. M. Reis, S. Willshaw, and T. Mullin, "Negative poisson's ratio behavior induced by an elastic instability," *Advanced Materials*, vol. 22, no. 3, pp. 361–366, 2010.

[9] R. S. Lakes, "Negative-poisson's-ratio materials: Auxetic solids," *Annual Review of Materials Research*, vol. 47, no. 1, pp. 63–81, 2017.

[10] X. Yu, J. Zhou, H. Liang, Z. Jiang, and L. Wu, "Mechanical metamaterials associated with stiffness, rigidity and compressibility: A brief review," *Progress in Materials Science*, vol. 94, pp. 114–173, 2018.

[11] M. A. Wadee, A. T. M. Phillips, and A. Bekele, "Effects of disruptive inclusions in sandwich core lattices to enhance energy absorbency and structural isolation performance," *Frontiers in Materials*, vol. 7, 2020.

[12] H. Yang and L. Ma, "1d and 2d snapping mechanical metamaterials with cylindrical topology," *International Journal of Solids and Structures*, vol. 204-205, pp. 220–232, 2020.

[13] A. Zolfagharian, M. Bodaghi, R. Hamzehei, L. Parr, M. Fard, and B. F. Rolfe, "3d-printed programmable mechanical metamaterials for vibration isolation and buckling control," *Sustainability*, vol. 14, no. 11, 2022.

[14] S. Liu, G. Peng, and K. Jin, "Design and characteristics of a novel qzs vibration isolation system with origami-inspired corrector," *Nonlinear Dynamics*, vol. 106, pp. 255–277, Sep 2021.

[15] D. A. Debeau, C. C. Seepersad, and M. R. Haberman, "Impact behavior of negative stiffness honeycomb materials," *Journal of Materials Research*, vol. 33, pp. 290–299, Feb 2018.

[16] T. Frenzel, C. Findeisen, M. Kadic, P. Gumbsch, and M. Wegener, "Tailored buckling microlattices as reusable light-weight shock absorbers," *Advanced Materials*, vol. 28, no. 28, pp. 5865–5870, 2016.

[17] D. Restrepo, N. D. Mankame, and P. D. Zavattieri, "Phase transforming cellular materials," *Extreme Mechanics Letters*, vol. 4, pp. 52–60, 2015.

[18] T. Mukhopadhyay, J. Ma, H. Feng, D. Hou, J. M. Gattas, Y. Chen, and Z. You, "Programmable stiffness and shape modulation in origami materials: Emergence of a distant actuation feature," *Applied Materials Today*, vol. 19, p. 100537, 2020.

[19] C. Cai, J. Zhou, L. Wu, K. Wang, D. Xu, and H. Ouyang, "Design and numerical validation of quasi-zero-stiffness metamaterials for very low-frequency band gaps," *Composite Structures*, vol. 236, p. 111862, 03 2020.

[20] J.-M. Battini, "Co-rotational beam elements in instability problems," 05 2002.

[21] S. p. Timoschenko and J. m. Gere, *Theory of elastic stability*. McGraw Hill Book, 2 ed., 1985.

[22] L. Mizzi, D. Attard, R. Gatt, K. K. Dudek, B. Ellul, and J. N. Grima, "Implementation of periodic boundary conditions for loading of mechanical metamaterials and other complex geometric microstructures using finite element analysis," *Engineering with Computers*, vol. 37, pp. 1765–1779, Jul 2021.

[23] Penguian, "Nurbs toolbox by d.m. spink." https://www.mathworks.com/matlabcentral/fileexchange/26390-nurbs-toolbox-by-d-m-spink, 2024. MATLAB Central File Exchange. Retrieved January 30, 2024.

[24] S. Farah, D. G. Anderson, and R. Langer, "Physical and mechanical properties of pla, and their functions in widespread applications — a comprehensive review," *Advanced Drug Delivery Reviews*, vol. 107, pp. 367–392, 2016. PLA biodegradable polymers.

[25] W. T. Koiter, *a translation of the stability of elastic equilibrium reference*. Air Force Flight Dynamics Laboratory, Air Force Systems Command, United States Air Force, Wright-Patterson Air Force Base, 1970.

4 Conclusion

This study presents a novel method for creating neutral stability in metamaterials. This is done by employing two identical elements that possess constant force-displacement behavior. These two elements are mirrored and pre-tensioned such that the constant force regions align and result in a constant zero force region, creating neutral stability.

A beam cross-section optimisation was conducted to find the optimal cross-section for the best constant force performance. The optimized solutions showed nearly constant force behavior but not a perfect one.

Prototypes were made and experimentally tested to validate this method of creating neutral stability. Discrepancies were observed between the simulations and the experimental results, which can be partially explained by manufacturing uncertainties. Even though perfect neutral stability was not achieved, the experiments proved that the method could work if a perfect constant force element could be manufactured.

The results give confidence that this method can be applied to other constant force mechanisms to create neutrally stable metamaterials.

A

Appendix A - Test setup design

The experimental test setup consists of multiple PLA 3D-printed parts. This appendix will discuss the design and dimensions of the parts. The test setup consists of a linear rail guide for movement in the x-direction, with the unit cell mounted on the rail. An overview of the test setup is shown in Figure A.1.

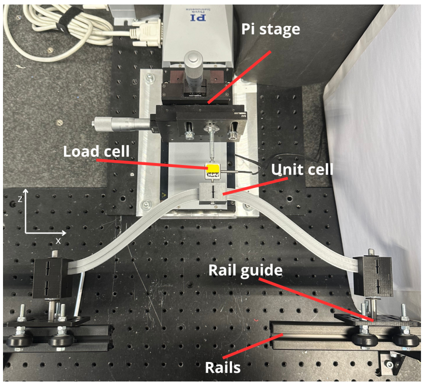

Figure A.1: Overview of the test setup

The rails are constructed with Thorlabs XE25L500/M profiles. These profiles are connected with Thorlabs RM1G cubes. The whole structure is mounted to the breadboard with Thorlabs XE25A90 angle brackets. The height of the horizontal beam with respect to the breadboard is adjusted such that it is in line with the load cell.

The rail guide consists of 3 Creality v-slot wheels and a v-slot profile. The v-slot profile is 3D-printed

Figure A.2: Test setup rails

and the dimensions are displayed in Figure A.3. The v-slot wheels are connected with m5 bolts and nuts to the 5mm diameter holes and the 5.05mm diameter slit.

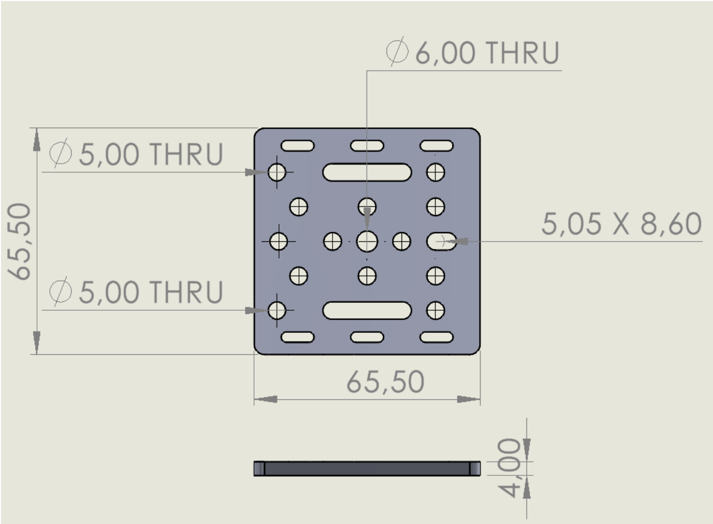

Figure A.3: Dimensions of v-slot profile in milimeters

The unit cell is also connected to v-slot profiles with a 6mm diameter steel axle that is pressed-fit in the 6mm hole of the v-slot profile. The geometric cut-out block has a hole through the middle with a ball bearing in it such that the steel axle can be connected to the block while keeping the rotation around the axle free. To prevent the block from moving up or down the axle two internal tooth washers are applied on the top and bottom of the block. An impression of the complete rail guide is shown in Figure A.4.

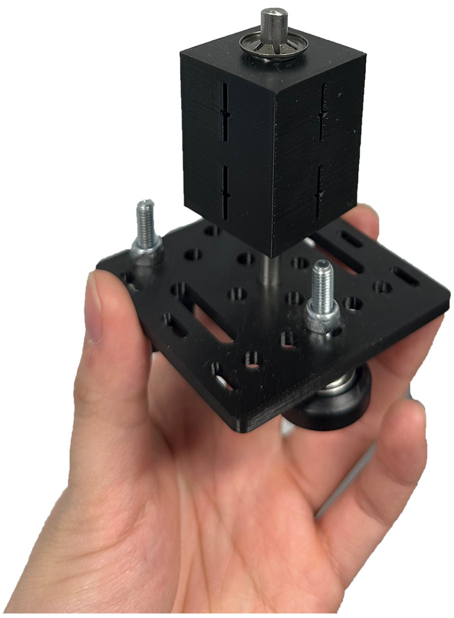

Figure A.4: Rail guide with unit cell attachment

Figure A.5 shows the dimensions of two different geometric cut-out blocks. Figure A.5a is the block connected to the V-slot and Figure A.5b is the block connected to the Pi-stage.

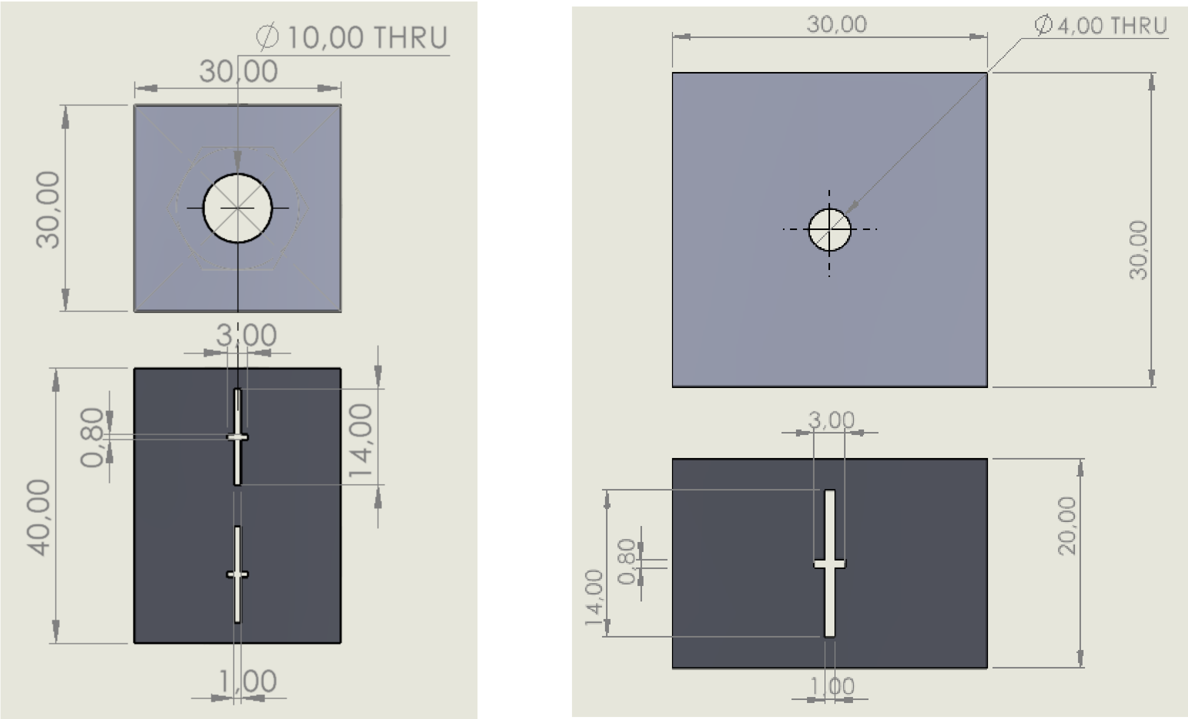

(a) Dimensions of the block connected to the v-slot profile

(b) Dimensions of the block connected to the Pi-stage

Figure A.5: Dimensions of the geometric cut-out block

B

Appendix B - Combined optimisation case

Optimization was conducted only on the beam's cross-section because optimizing the spline shape would give an unrealistic shape. The scenario involving simultaneous optimization of both the cross-section and spline shape was not explored before the experimental stage. Presented here are the findings from the integrated optimization case.

The upper and lower boundaries of the cross-section are set to the same values as the single optimization case. The boundaries of the NURBS coefficients are set as shown in Figure B.1

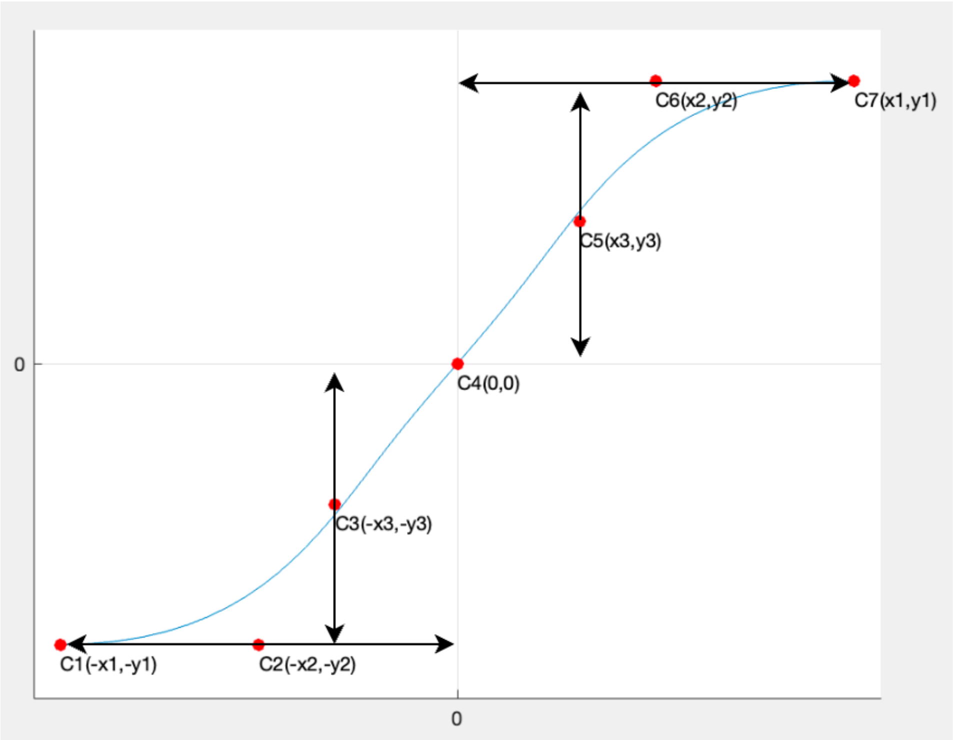

Figure B.1: Upper and lower boundaries of the NURBS coefficients for optimization

However, combining the optimization cases does not significantly change the outcome compared to the isolated cross-section optimization. The changes are sub-millimeter which is not noticeable in the results.

C

Appendix C - Other concepts and ideas

At the initial stage of this study, multiple designs were considered as starting points. The designs do have potential but require extra research to realize the goal of neutral stability.

C.1. Concept 1

The first concept is based on a squared shape that is pre-tensioned with some kind of hook mechanism. The pre-tension makes the square bi-stable as can be seen in Figure C.1. The idea to make this unit neutrally stable is based on the fact that the total stiffness of the unit cell is a combination of the linear material stiffness and the nonlinear geometry stiffness. So if the unit cell is bi-stable it can in theory be made into a constant force unit cell by increasing the material stiffness, such as by increasing the thickness.

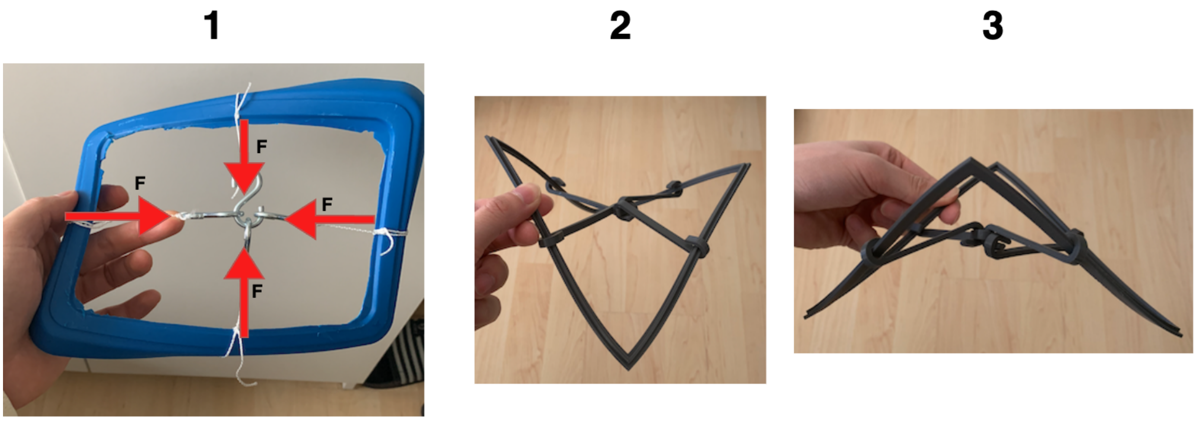

Figure C.1: 1) shows the top view of the concept. It shows a rectangular circumference which is pre-tensioned with a hook. 2) shows a side view of the unit cell in stable equilibrium position 1. 3) shows the side view in stable equilibrium position 2.

C.2. Concept 2

The second concept uses the same principle as concept 1 to achieve neutral stability. However, the method of pre-tensioning differs. Concept 2 uses a squared profile that has a cut and is slightly bent as shown in Figure C.2. By attaching both open ends it will be pre-tensioned and possess bi-stable behavior. Same as concept 1 the material stiffness can be increased to achieve a constant force behavior and eventually neutral stability.

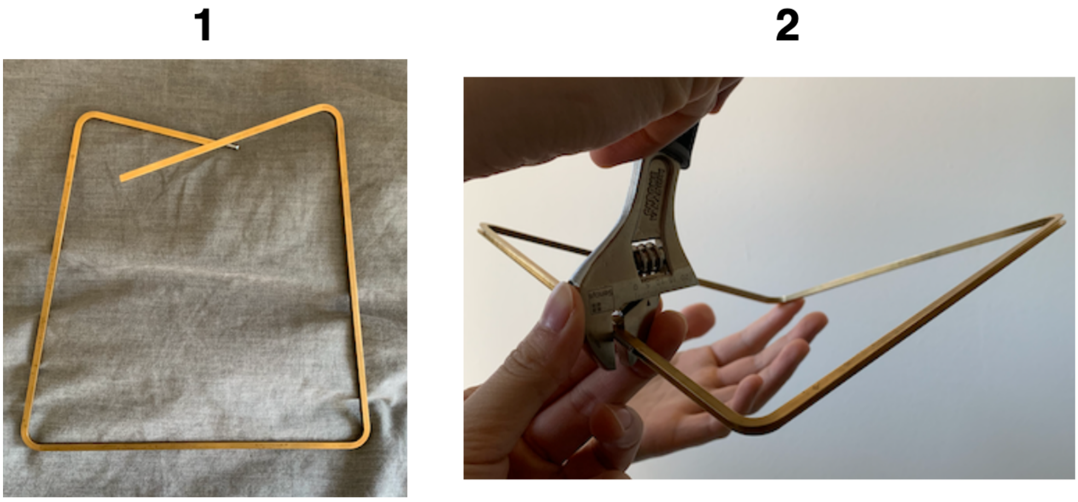

Figure C.2: 1) shows the top view of the unit cell. 2) shows the side view of the unit cell. The open ends are held together with an adjustable wrench.

C.3. Concept 3

The design of concept 3 is inspired by the origami hypar[5]. The origami hypar is bistable and made from a sheet of plastic or paper, but this concept is 3D printed and has a larger thickness than the original origami hypar. The increase in thickness changes the bi-stable behavior into a constant-force behavior. When connecting another mirrored cell and applying pre-tension, the combined unit cell should in theory be neutrally stable. Different views of the design are shown in Figure C.3.

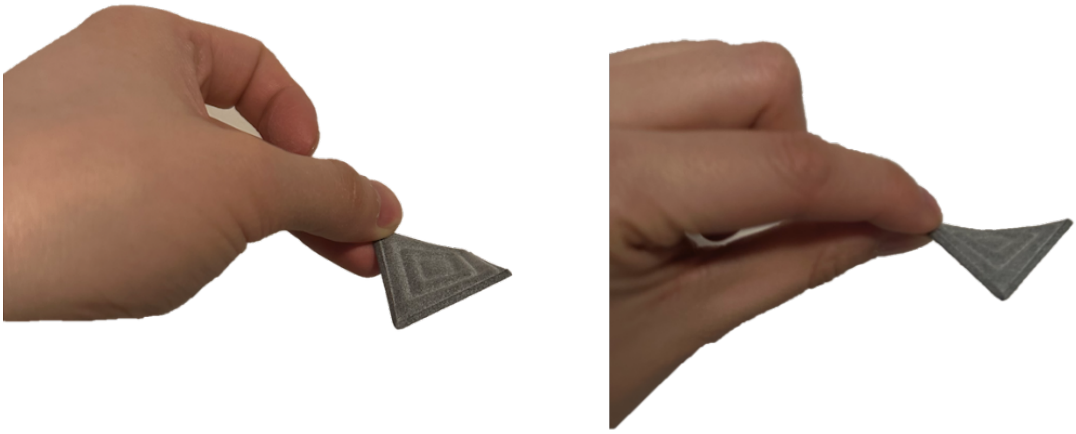

Figure C.3: Isometric view and side view of concept 3

C.4. Alternative beam

In the literature, an interesting beam design was made by Zhang et al.[21]. This beam has programmable constant force properties. The beam has a certain curve and uses a rectangle as a cross-section, so it seems to be easier to manufacture. This beam might serve as an alternative to the design we initially proposed, but further investigation is necessary to verify its feasibility. Figure C.4 shows the force-displacement behavior of the beam and a variation of the curved beam.

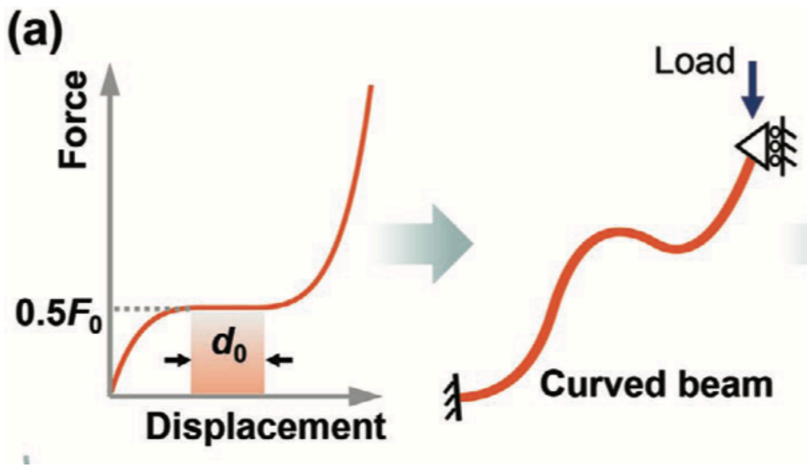

Figure C.4: Constant force beam design by Zhang et al. Retrieved from [21]

D

Appendix D - Sign switching Poisson's Ratio

A unique property was observed in this metamaterial design which was not intended. It has to do with Poisson's ratio behavior. When a certain elastic elongation is applied to an isotropic material, the length in the longitudinal direction is extended, while the length in the lateral direction is contracted. This behavior can be found in normal materials with a Poisson's ratio larger than zero. The Poisson's ratio is as follows:

$$v = -\frac{\epsilon_{lat}}{\epsilon_{long}} \tag{D.1}$$

Here ϵ_{lat} and ϵ_{long} are the lateral strain and longitudinal strain respectively.

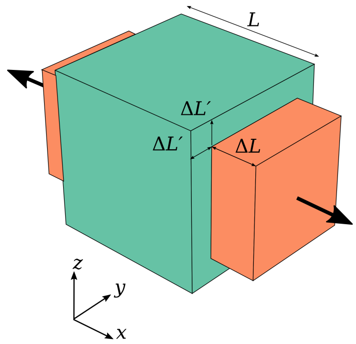

Figure D.1: Illustration of the deformation in the lateral direction when a material is elongated. Retrieved from [16]

A small 3x3x1 version of this metamaterial was built to observe the behavior of the deformations. This prototype is shown in Figure D.2. When compression is applied in the Z-direction, the metamaterial will extend in the x-direction and contract in the y-direction. This deformation is caused by the buckling of the beams. Figure D.3 shows the deformed metamaterial. In isotropic materials, the strain resulting from the compression would be the same for the x and y directions. Using Equation D.2 results in a positive Poisson's ratio for the lateral x-direction and a negative Poisson's ratio for the lateral y-direction.

$$v_{zx} = -\frac{\epsilon_x}{\epsilon z}, v_{zy} = -\frac{\epsilon_y}{\epsilon z} \tag{D.2}$$

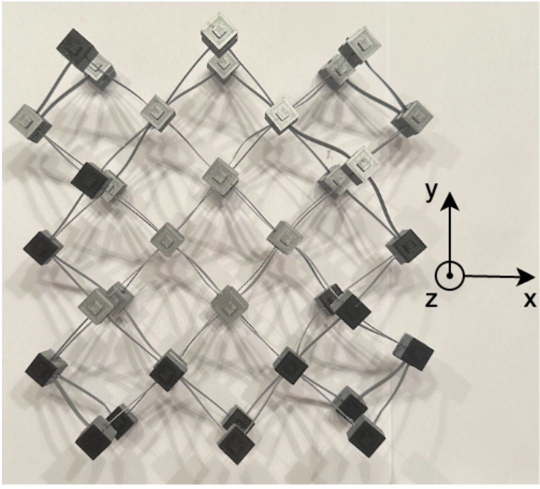

Figure D.2: 3x3x1 metamaterial in undeformed state

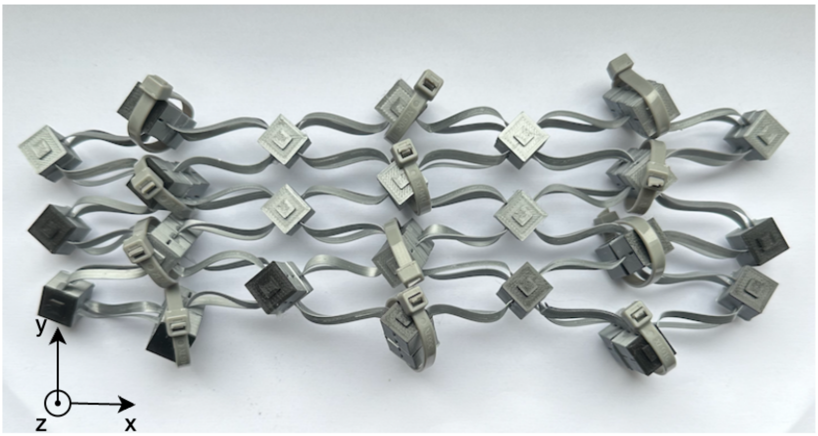

Figure D.3: Metamaterial in deformed state with elongation in x-direction and contraction in y direction

However, the beams have a second buckling mode, causing the deformations to be the other way around. Instead of a contraction in the y direction, the x-direction will be contracted and the y-direction will be extended. This deformation is shown in Figure D.4. Analyzing the Poisson's ratio it can be noticed that instead of having a positive Poisson's ratio for the lateral x-direction and a negative Poisson's ratio for the lateral y-direction, the Poisson's ratio will be negative for x and positive for y. This behavior indicated that the metamaterial possesses a sign-switching Poisson's ratio behavior depending on which way the beam buckles.

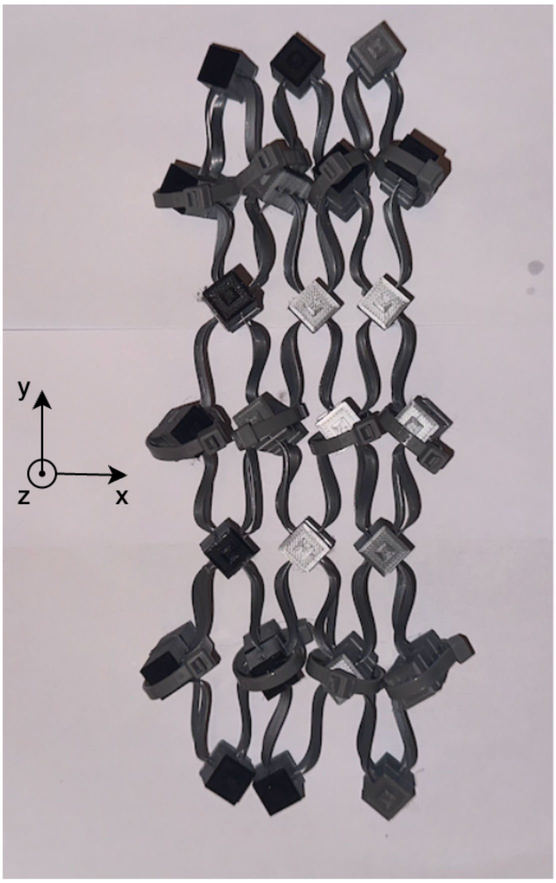

Figure D.4: Metamaterial in deformed state with contraction in x-direction and elongation in y-direction

E

Appendix E- Matlab code

E.1. Objective function

The objective function for the optimisation:

```
function objective = mean_absolute_deviation_CA(param)

   param_1=param(1)
   param_2=param(2)
   param_3=param(3)
   param_4=param(4)

    coefs= [0 37.5 51.9 75 98.1 112.5 150;
        0 0 21 42 63.375 84.375 84.375]/1000;




    nx=1;
    ny=1;
    nz=1;
    % Update the nrbs structure with the new coefficients
    [x, y, z, elementNodes] = create_single_unit_cell_opt(coefs);
    [x, y, z, elementNodes] = replicate_unit_cells_opt(nx, ny, nz,x,y,z,coefs);

    % (Include the existing script here with the updated nrbs structure)
    par.nTimestep    = 500;
    par.nIter        = 100;
    par.conv         = 5e-5;
    par.plots        = 'off';
    par.getKend      = 0;

    nbeam = numel(x);
m.X = [x, y, z, zeros(3, nbeam)'];

% Update the m.elementNodes matrix with the new node connections
m.elementNodes = elementNodes;
m.numberNodes        = size(m.X,1);
m.numberElements     = size(m.elementNodes,1);
m.eqn                = 6*m.numberNodes;
m.x                  = reshape(m.X',m.eqn,1) ;



```

```
%PLA
m.E          =   3.2e9*ones(1,m.numberElements);
m.G          =   1.1e9*ones(1,m.numberElements);



m = DefineCrossSection(m,'Cruciform', param_1, param_2, param_3, param_4);



%%Use this for a single orientation point
CSO = [ 0 0 10000]';    % cross section orientation. Is the point towards which e03 points. Used to be fixed [0.00001 0.000001 1]'
m.GuideCurve = repmat(CSO,1,m.numberNodes);
m.guidecurve = reshape(m.GuideCurve,3*m.numberNodes,1) ;
%     %%Use this to specify an orientation curve
%     m.GuideCurve = m.X(:,1:3)';
%     m.GuideCurve(1,:) = m.GuideCurve(1,:) + param_1;
%     m.GuideCurve(2,:) = m.GuideCurve(2,:) + param_2;
%     m.GuideCurve(3,:) = m.GuideCurve(3,:) + param_3;
%     m.guidecurve = reshape(m.GuideCurve,3*m.numberNodes,1) ;

%% core

for e = 1:m.numberElements
%     m_beams.tr1(:,:,e)         = eye(3)*rotRo1(m_beams.X(e+1,1:3)'-m_beams.X(e,1:3)');
%     m_beams.tr2(:,:,e)         = eye(3)*rotRo1(m_beams.X(e+2,1:3)'-m_beams.X(e+1,1:3)');

%modified rotRo1 met richting e03 naar bepaald punt (niet de snelste versie)
x21=(m.X(m.elementNodes(e,2),1:3)'-m.X(m.elementNodes(e,1),1:3)');
e01      = (x21)/norm(x21);
%     e03star = veccross(e01,[0.00001 0.000001 1]');
e03star = cross(e01, m.guidecurve(3*(m.elementNodes(e,1)-1)+[1:3]) - m.X(m.elementNodes(e,1),1:3)');
e03      = e03star/norm(e03star);
e02      = cross(e03,e01);
%e03 e02 roteren hier voorzichtig



Ro       = [e01 e02 e03];        % voor eqn 4.28

m.tr1(:,:,m.elementNodes(e,1))         = eye(3)*Ro;
m.tr2(:,:,m.elementNodes(e,1))         = eye(3)*Ro;
end
m.tr1(:,:,m.numberElements)         = eye(3)*Ro;
m.tr2(:,:,m.numberElements)         = eye(3)*Ro;

% m_beams.tr1               = repmat(eye(3),1,1,m_beams.numberElements);
% m_beams.tr2               = repmat(eye(3),1,1,m_beams.numberElements);
m.Rg1                 = repmat(eye(3),1,1,m.numberElements);%repmat({eye(3)},m_beams.numberElements,1);
m.Rg2                 = repmat(eye(3),1,1,m.numberElements);

m.D                   = zeros(6,m.numberNodes)';
m.d                   = zeros(m.eqn,1);

% mex('-O','-I"C:\Program','Files','(x86)\Microsoft','Visual','Studio','14.0\VC\include"','COMP
```

```
    'AssembleMatricesBeams', ['-Deqn=' num2str(m_beams.eqn)], ['-Dnel='
    num2str(m_beams.numberElements)] )
%
    mex('-O','-I"C:\Program','Files','(x86)\Microsoft','Visual','Studio','14.0\VC\include"','COMP
    'StrainEnergyCRbeams', ['-Deqn=' num2str(m_beams.eqn)], ['-Dnel='
    num2str(m_beams.numberElements)]  )
plotBeams(m)
try
%% BOUNDARY CONDITIONS on begin- and endpoint
height = coefs(2,7);
indices_max=find(z==max(z));
indices_min=find(z==min(z));
pointconstraints=zeros(6,m.numberNodes); %creates a 6 by N array with zeros

allIndices = [indices_min; indices_max];%all top and bottom nodes

% Set corresponding elements in pointconstraints to 1
pointconstraints([1 2 3 4 5 6], 1) = 1; % constraint in node 1 to prevent shifting
pointconstraints([3 4 5], allIndices) = 1;% contraints for the top and bottom
    nodes

dofs.bc = find(pointconstraints)';
dofs.dp = zeros(sum(pointconstraints,'all'),1);


Fe  = zeros(m.eqn,1);%geleidelijke kracht toepassen
PreFe  = zeros(m.eqn,1); %instant kracht


count = 0;
activeconstraints = [];
for i = 1:size(pointconstraints, 2)
    for j = 1:size(pointconstraints, 1)
        if pointconstraints(j,i) == 1
            count = count + 1;
            if j == 3 && ismember(i, indices_max)
                activeconstraints = [activeconstraints, count];
            end
        end
    end
end

dofs.dp(activeconstraints) = -1*height; %displacements on the 4e en 8e dof.

dofs.all    = (1:m.eqn)';
%dofs.bc      = bc(~isnan([dofs.dp]));
%dofs.dp      = dofs.dp(~isnan([dofs.dp]));
dofs.R       =
    sparse(1:length(dofs.bc),[dofs.bc],1+0*dofs.bc,length(dofs.bc),m.eqn);
def='def';
[history, m] = solveNONLINstaticCOR(m,dofs,par,Fe,PreFe);

for i=1: length(history)
   RF(i,:) =  [history(i).RF(activeconstraints)] ;
end

    % Calculate the mean absolute deviation
    displacement = linspace(0, -dofs.dp(activeconstraints(1)), par.nTimestep);
    startIndex= length(RF)*0.3;
    displacement=displacement(1,startIndex:end)';
    force = -RF(startIndex:end, 1); % beware if you change the timestep
```

```



%% objective functions
fmean=mean(force);
objective=sum(((force-fmean)/fmean).^2) %original


catch ME
        disp(['Error in Param_opt: ' ME.message]);
        objective = NaN; % Return NaN when there's an error
end









end
```

E.2. Cross-section optimiser model

Code for the cross-section optimiser

```
clear all
%
%% Fmincon

%Define initial guess for the parameters
initial_guess = [0.0132641873479819 0.000785728297885106 0.00275747010260366
    0.000566292405809865]  ;

% Define constraints
% If you don't have any constraints, you can use empty matrices []
A = [];  % Linear inequality constraints
b = [];  % Linear inequality constraints
Aeq = [];  % Linear equality constraints
beq = [];  % Linear equality constraints
lb = [0.0001 0.0001 0.0001 0.0001];   %lower bounds
ub = [20e-3 1.5e-3 20e-3 1.5e-3];  % Upper bounds


% Call fmincon

%options = optimoptions('fmincon','Display','iter-detailed');

[optimal_params, exitflag ,fval] = fmincon(@mean_absolute_deviation_CA,
    initial_guess, A, b, Aeq, beq, lb, ub,[]);

% Print the results
fprintf('The optimal parameters are: %.4f,%.4f\n', optimal_params(1),
    optimal_params(2),optimal_params(3),optimal_params(4));
fprintf('The minimal objective value is: %.4f\n', fval);
```

E.3. Function for creating a single unit cell

Code for creating a single unit cell

```
function [x, y, z, elementNodes, elements_side,height] = create_single_unit_cell_test()

%% NRBS Creation

diagonal = 0.08;
elements_side = 20;
coefs = [0 37.5 51.9 75 98.1 112.5 150;
         0 0 21 42 63.375 84.375 84.375]/1000;
height = coefs(2,7);

knots = [0 0 0 0 0.4 0.5 0.6 1 1 1 1];% Define the knot sequence (degree 3, so 4 repeated knots at the beginning and end)

nrbs = nrbmak(coefs, knots);% Create the NURBS structure

param_values = linspace(0, 1, elements_side);% Define the parameter values

curve_points = nrbeval(nrbs, param_values);% Evaluate the NURBS curve at the parameter values, outputs cartesian coordinates


%% define lowerspline 1
x_i = curve_points(1, :)';% x Initial
z_i = curve_points(2, :)';% y initial
y_i = zeros(elements_side, 1); % z initial


%rotate
rotation_angle_degrees = 45;
rotation_angle_radians = deg2rad(rotation_angle_degrees);

%rotation matrix
Rz = [cos(rotation_angle_radians), -sin(rotation_angle_radians), 0;
      sin(rotation_angle_radians), cos(rotation_angle_radians), 0;
      0, 0, 1];

% Perform the rotation
xyz = [x_i, y_i, z_i]; % initial coordinates in a matrix, every coordinate is a column
xyz_rotated = xyz * Rz;

% Store the rotated coordinates
x_r1 = xyz_rotated(:, 1);
y_r1 = xyz_rotated(:, 2);
z_r1 = xyz_rotated(:, 3);

%% define spline lower 2
rotation_angle_degrees = 90;
rotation_angle_radians = deg2rad(rotation_angle_degrees);
Rz = [cos(rotation_angle_radians), -sin(rotation_angle_radians), 0;
      sin(rotation_angle_radians), cos(rotation_angle_radians), 0;
      0, 0, 1];

% Shift the spline to origin
x_shifted = x_r1 - max(x_r1);
y_shifted= y_r1- min(y_r1);

%perform rotation
xyz_r1=[x_shifted,y_shifted,z_r1];
xyz_r1_rotated=xyz_r1*Rz;
```

```
%shift back
xyz_r1_rotated(:, 1) = xyz_r1_rotated(:, 1) + max(x_r1);
xyz_r1_rotated(:, 2) = xyz_r1_rotated(:, 2) + min(y_r1);

x_r2 = xyz_r1_rotated(:, 1);
y_r2 = xyz_r1_rotated(:, 2);
z_r2 = xyz_r1_rotated(:, 3);
% Define spline upper

x_i = curve_points(1, :)';
z_i = curve_points(2, :)';

% Define y_i variable
y_i = zeros(elements_side, 1);


%rotate
rotation_angle_degrees = -45;
rotation_angle_radians = deg2rad(rotation_angle_degrees);

% Define the rotation matrix
Rz = [cos(rotation_angle_radians), -sin(rotation_angle_radians), 0;
      sin(rotation_angle_radians), cos(rotation_angle_radians), 0;
      0, 0, 1];

% % Shift the spline so that the right end is at the origin
% x_shifted = x_i - max(x_i);

% Perform the rotation
xyz = [x_i, y_i, z_i];
xyz_rotated = xyz * Rz;

% % Shift the rotated spline back to its original position
% xyz_rotated(:, 1) = xyz_rotated(:, 1) - max(x_i);

% Store the rotated coordinates
x_r3 = xyz_rotated(:, 1);
y_r3 = xyz_rotated(:, 2);
z_r3 = xyz_rotated(:, 3);

% Spline upper 2
rotation_angle_degrees = -90;
rotation_angle_radians = deg2rad(rotation_angle_degrees);
Rz = [cos(rotation_angle_radians), -sin(rotation_angle_radians), 0;
      sin(rotation_angle_radians), cos(rotation_angle_radians), 0;
      0, 0, 1];
% Shift the spline to origin
x_shifted = x_r3 - max(x_r3);
y_shifted= y_r3- max(y_r3);

%perform rotation
xyz_r3=[x_shifted,y_shifted,z_r3];
xyz_r3_rotated=xyz_r3*Rz;

%shift back
xyz_r3_rotated(:, 1) = xyz_r3_rotated(:, 1) + max(x_r3);
xyz_r3_rotated(:, 2) = xyz_r3_rotated(:, 2) + max(y_r3);
x_r4 = xyz_r3_rotated(:, 1);
y_r4 = xyz_r3_rotated(:, 2);
z_r4 = xyz_r3_rotated(:, 3);
```

```


% define x y z
x=[x_r1' flip(x_r2') x_r4' flip(x_r3')]';
y=[y_r1' flip(y_r2') y_r4' flip(y_r3')]';
z=[z_r1' flip(z_r2') z_r4' flip(z_r3')]';

% Find the maximum Z-coordinate value
max_z = max(z);

% Define the gap between the original unit cell and the mirrored unit cell
gap = height; % Set the desired gap value!!!!!!!!!!!!!!!!!!!!!!

% Mirror the Z-coordinates
z_mirrored = (max_z + gap) - z;

%Final unit cell geometry
x = [x; x];
x([elements_side+1 2*elements_side+1 3*elements_side+1 4*elements_side
    4*elements_side+1 5*elements_side 5*elements_side+1 6*elements_side+1
    7*elements_side 7*elements_side+1])=[];
y = [y; y];
y([elements_side+1 2*elements_side+1 3*elements_side+1 4*elements_side
    4*elements_side+1 5*elements_side 5*elements_side+1 6*elements_side+1
    7*elements_side 7*elements_side+1])=[];
z = [z; z_mirrored];
z([elements_side+1 2*elements_side+1 3*elements_side+1 4*elements_side
    4*elements_side+1 5*elements_side 5*elements_side+1 6*elements_side+1
    7*elements_side 7*elements_side+1])=[];

elementNodes_lower = [1:4*elements_side-5;2:4*elements_side-4];
elementNodes_upper=
    [4*elements_side-3:8*elements_side-11;4*elements_side-2:8*elements_side-10];%nodes
    worden nog geconnect met elkaar ipv intersect
elementNodes_intersect= [[5*elements_side-6 elements_side 7*elements_side-9
    3*elements_side-2 4*elements_side-4 8*elements_side-10];[elements_side
    5*elements_side-5 3*elements_side-2 7*elements_side-8 1 4*elements_side-3]];

elementNodes=[elementNodes_lower elementNodes_upper elementNodes_intersect]';
elementNodes([5*elements_side-7 7*elements_side-10],:)=[];

% x = x + (rand(length(x),1)-0.5)*40*10^-4;
% y = y + (rand(length(x),1)-0.5)*40*10^-4;
x = x + (rand(length(x),1)-0.5)*10^-4;
y = y + (rand(length(x),1)-0.5)*10^-4;

end
```

E.4. Function for creating metamaterial (unit cell tessellation)

Code for creating metamaterial, but it is a little buggy.

```
function [x, y, z, elementNodes,elements_side,height] =
    replicate_unit_cells_test(nx, ny, nz)
  [x, y, z, elementNodes,elements_side,height] = create_single_unit_cell_test();
% function [x, y, z, elementNodes] = replicate_unit_cells(nx, ny, nz,x,y,z,coefs)
%   [x, y, z, elementNodes] = create_single_unit_cell(coefs);
    x_max = max(x);
    y_max = max(y);
    z_max = max(z);

```

```
    x_all = [];
    y_all = [];
    z_all = [];
    elementNodes_all = [];

    n_nodes = size(x, 1);
    for k = 0:(nz-1)
        for j = 0:(ny-1)
            for i = 0:(nx-1)
                x_temp = x + i * x_max;
                y_temp = y + j * 2*y_max;
                z_temp = z + k * z_max;
                elementNodes_temp = elementNodes + (i + j * nx + k * nx * ny) *
                    n_nodes;

                x_all = [x_all; x_temp];
                y_all = [y_all; y_temp];
                z_all = [z_all; z_temp];
                elementNodes_all = [elementNodes_all; elementNodes_temp];
            end
        end
    end

    % Remove overlapping nodes
    tol = 1e-6;
    rounded_coords = round([x_all, y_all, z_all] / tol) * tol;
    [C, ~, ic] = unique(rounded_coords, 'rows', 'stable');
    x = C(:, 1);
    y = C(:, 2);
    z = C(:, 3);

    % Update the elementNodes using the index array ic
    elementNodes = ic(elementNodes_all);

    % Remove duplicate node connections
    duplicate_rows = (elementNodes(:, 1) == elementNodes(:, 2));
    elementNodes(duplicate_rows, :) = [];



end
```

Bibliography

[1] Katia Bertoldi et al. "Flexible mechanical metamaterials". In: *Nature Reviews Materials* 2.11 (Oct. 2017), p. 17066. ISSN: 2058-8437. DOI: 10.1038/natrevmats.2017.66. URL: https://doi.org/10.1038/natrevmats.2017.66.

[2] Katia Bertoldi et al. "Negative Poisson's Ratio Behavior Induced by an Elastic Instability". In: *Advanced Materials* 22.3 (2010), pp. 361–366. DOI: https://doi.org/10.1002/adma.200901956. eprint: https://onlinelibrary.wiley.com/doi/pdf/10.1002/adma.200901956. URL: https://onlinelibrary.wiley.com/doi/abs/10.1002/adma.200901956.

[3] Changqi Cai et al. "Design and numerical validation of quasi-zero-stiffness metamaterials for very low-frequency band gaps". In: *Composite Structures* 236 (Mar. 2020), p. 111862. DOI: 10.1016/j.compstruct.2020.111862.

[4] David A. Debeau, Carolyn C. Seepersad, and Michael R. Haberman. "Impact behavior of negative stiffness honeycomb materials". In: *Journal of Materials Research* 33.3 (Feb. 2018), pp. 290–299. ISSN: 2044-5326. DOI: 10.1557/jmr.2018.7. URL: https://doi.org/10.1557/jmr.2018.7.

[5] E.T. Filipov and M. Redoutey. "Mechanical characteristics of the bistable origami hypar". In: *Extreme Mechanics Letters* 25 (2018), pp. 16–26. ISSN: 2352-4316. DOI: https://doi.org/10.1016/j.eml.2018.10.001. URL: https://www.sciencedirect.com/science/article/pii/S2352431618300907.

[6] Tobias Frenzel et al. "Tailored Buckling Microlattices as Reusable Light-Weight Shock Absorbers". In: *Advanced Materials* 28.28 (2016), pp. 5865–5870. DOI: https://doi.org/10.1002/adma.201600610. eprint: https://onlinelibrary.wiley.com/doi/pdf/10.1002/adma.201600610. URL: https://onlinelibrary.wiley.com/doi/abs/10.1002/adma.201600610.

[7] Pengcheng Jiao et al. "Mechanical metamaterials and beyond". In: *Nature Communications* 14.1 (Sept. 2023), p. 6004. ISSN: 2041-1723. DOI: 10.1038/s41467-023-41679-8. URL: https://doi.org/10.1038/s41467-023-41679-8.

[8] R.S. Lakes et al. "Extreme damping in composite materials with negative-stiffness inclusions". In: *Nature* 410.6828 (2001), pp. 565–567. DOI: 10.1038/35069035. URL: https://www.scopus.com/inward/record.uri?eid=2-s2.0-0035967154&doi=10.1038%2f35069035&partnerID=40&md5=4b2d2de5d2ef7693983fce5809230092.

[9] Roderic S. Lakes. "Negative-Poisson's-Ratio Materials: Auxetic Solids". In: *Annual Review of Materials Research* 47.1 (2017), pp. 63–81. DOI: 10.1146/annurev-matsci-070616-124118. eprint: https://doi.org/10.1146/annurev-matsci-070616-124118. URL: https://doi.org/10.1146/annurev-matsci-070616-124118.

[10] Shiwei Liu, Gaoliang Peng, and Kang Jin. "Design and characteristics of a novel QZS vibration isolation system with origami-inspired corrector". In: *Nonlinear Dynamics* 106.1 (Sept. 2021), pp. 255–277. ISSN: 1573-269X. DOI: 10.1007/s11071-021-06821-5. URL: https://doi.org/10.1007/s11071-021-06821-5.

[11] Hongye Ma et al. "A reusable metastructure for tri-directional energy dissipation". In: *International Journal of Mechanical Sciences* 214 (Jan. 2022), p. 106870. ISSN: 0020-7403. URL: https://www.sciencedirect.com/science/article/pii/S0020740321005919.

[12] Tanmoy Mukhopadhyay et al. "Programmable stiffness and shape modulation in origami materials: Emergence of a distant actuation feature". In: *Applied Materials Today* 19 (2020), p. 100537. ISSN: 2352-9407. DOI: https://doi.org/10.1016/j.apmt.2019.100537. URL: https://www.sciencedirect.com/science/article/pii/S2352940719306572.

[13] David Restrepo, Nilesh D. Mankame, and Pablo D. Zavattieri. “Phase transforming cellular materials”. In: *Extreme Mechanics Letters* 4 (2015), pp. 52–60. ISSN: 2352-4316. DOI: https://doi.org/10.1016/j.eml.2015.08.001. URL: https://www.sciencedirect.com/science/article/pii/S2352431615000929.

[14] James Utama Surjadi et al. “Mechanical Metamaterials and Their Engineering Applications”. In: *Advanced Engineering Materials* 21.3 (2019), p. 1800864. DOI: https://doi.org/10.1002/adem.201800864. eprint: https://onlinelibrary.wiley.com/doi/pdf/10.1002/adem.201800864. URL: https://onlinelibrary.wiley.com/doi/abs/10.1002/adem.201800864.

[15] M. Ahmer Wadee, Andrew T. M. Phillips, and Adam Bekele. “Effects of Disruptive Inclusions in Sandwich Core Lattices to Enhance Energy Absorbency and Structural Isolation Performance”. In: *Frontiers in Materials* 7 (2020). ISSN: 2296-8016. DOI: 10.3389/fmats.2020.00134. URL: https://www.frontiersin.org/articles/10.3389/fmats.2020.00134.

[16] Wikipedia. *Poisson’s ratio*. 2024. URL: https://en.wikipedia.org/wiki/Poisson%27s_ratio.

[17] Lingling Wu et al. “A brief review of dynamic mechanical metamaterials for mechanical energy manipulation”. In: *Materials Today* 44 (2021), pp. 168–193. ISSN: 1369-7021. DOI: https://doi.org/10.1016/j.mattod.2020.10.006. URL: https://www.sciencedirect.com/science/article/pii/S1369702120303618.

[18] Hang Yang and Li Ma. “1D and 2D snapping mechanical metamaterials with cylindrical topology”. In: *International Journal of Solids and Structures* 204-205 (2020), pp. 220–232. ISSN: 0020-7683. DOI: https://doi.org/10.1016/j.ijsolstr.2020.08.023. URL: https://www.sciencedirect.com/science/article/pii/S0020768320303280.

[19] Hang Yang and Li Ma. “Angle-Dependent Transitions Between Structural Bistability and Multistability”. In: *Advanced Engineering Materials* 22.5 (2020), p. 1900871. DOI: https://doi.org/10.1002/adem.201900871. eprint: https://onlinelibrary.wiley.com/doi/pdf/10.1002/adem.201900871. URL: https://onlinelibrary.wiley.com/doi/abs/10.1002/adem.201900871.

[20] Xianglong Yu et al. “Mechanical metamaterials associated with stiffness, rigidity and compressibility: A brief review”. In: *Progress in Materials Science* 94 (2018), pp. 114–173. ISSN: 0079-6425. DOI: https://doi.org/10.1016/j.pmatsci.2017.12.003. URL: https://www.sciencedirect.com/science/article/pii/S0079642517301445.

[21] Quan Zhang, Dengke Guo, and Gengkai Hu. “Tailored Mechanical Metamaterials with Programmable Quasi-Zero-Stiffness Features for Full-Band Vibration Isolation”. In: *Advanced Functional Materials* 31.33 (2021), p. 2101428. DOI: https://doi.org/10.1002/adfm.202101428. eprint: https://onlinelibrary.wiley.com/doi/pdf/10.1002/adfm.202101428. URL: https://onlinelibrary.wiley.com/doi/abs/10.1002/adfm.202101428.

[22] Ali Zolfagharian et al. “3D-Printed Programmable Mechanical Metamaterials for Vibration Isolation and Buckling Control”. In: *Sustainability* 14.11 (2022). ISSN: 2071-1050. DOI: 10.3390/su14116831. URL: https://www.mdpi.com/2071-1050/14/11/6831.